True Nulls-Free Magnetoinductive Waveguides Using Alternate Coupling Polarities for Batteryless Dynamic Wireless Power Transfer Applications

Chawalit Rakluea, *Student Member, IEEE*, Apisak Worapishet, *Senior Member, IEEE*,
Sarawuth Chaimool, *Senior Member, IEEE*, Yan Zhao, *Senior Member, IEEE*,
and Prayoot Akkaraekthalin, *Member, IEEE*

***Abstract*—A dynamic wireless power transfer (DWPT) system using the conventional magnetoinductive (MI) waveguide suffers from periodic power nulls resulting from standing waves. Although numerous methods have been developed to mitigate the nulls, additional active circuitry was required, increasing the complexity. In this article, the MI waveguide with alternate magnetic coupling polarities between successive resonator cells is proposed for a true nulls-free DWPT system with no use of active components. Two configurations of the alternately coupled MI (ACMI) waveguide are developed—one with the incorporation of a quadrature-phase termination for a linear waveguide, and the other with the adoption of a circular waveguide. Extensive analysis of the generalized ACMI waveguide is provided, and the developed configurations are theoretically verified to maintain power transfer efficiency, independent of the free-positioned load. Practical implementation of DWPT systems using the linear and circular ACMI configurations with seven resonator cells at 13.56-MHz operation are experimentally demonstrated to exhibit no power transfer nulls and achieve up to fivefold reduction in efficiency variation, as compared to their MI counterparts. Comparisons with theoretical calculation are given for verification of the analysis integrity. An experimental model of a batteryless DWPT system is also demonstrated using the circular waveguide as accompanied by a video.**

***Index Terms*—Alternate coupling polarity, dynamic wireless power transfer (DWPT), magnetoinductive (MI) wave, nulls-free.**

Manuscript received August 10, 2021; revised November 14, 2021; accepted January 7, 2022. Date of publication January 25, 2022; date of current version April 28, 2022. This work was supported in part by the National Science Research and Innovation Fund and King Mongkut's University of Technology North Bangkok under Contract KMUTNB-FF-65-21, in part by the Rajamangala University of Technology Thanyaburi, Thailand, and in part by the Thailand Research Fund under Grant RSA6280056. Recommended for publication by Associate Editor O. Onar. *(Corresponding author: Apisak Worapishet.)*

Chawalit Rakluea and Prayoot Akkaraekthalin are with the Department of Electrical and Computer Engineering, Faculty of Engineering, King Mongkut's University of Technology North Bangkok, Bangkok 10800, Thailand (e-mail: chawalit@rmutt.ac.th; prayoot.a@eng.kmutnb.ac.th).

Apisak Worapishet is with the Mahanakorn Institute of Innovation, Mahanakorn University of Technology, Bangkok 10530, Thailand (e-mail: apisak@mut.ac.th).

Sarawuth Chaimool is with the Department of Electrical Engineering, Faculty of Engineering, Khon Kaen University, Khon Kaen 40002, Thailand (e-mail: jaounarak@gmail.com).

Yan Zhao is with the International School of Engineering, Faculty of Engineering, Chulalongkorn University, Bangkok 10330, Thailand (e-mail: yan.z@chula.ac.th).

This article has supplementary material provided by the authors and color versions of one or more figures available at https://doi.org/10.1109/TPEL.2022.3145579.

Digital Object Identifier 10.1109/TPEL.2022.3145579

I. Introduction

FOLLOWING its renewed interest in [1] more than one century after its inception by Tesla [2], the wireless power transfer (WPT) via coupled magnetic resonance has nowadays attracted a great deal of research attention with the frequency of operation ranging from kHz to a few MHz [3]–[30]. Its widespread utilization has nowadays spanned from stationary or localized wireless battery charging for consumer electronic gadgets [3]–[5], electric vehicles [6]–[8], and medical implants [9] to dynamic wireless power delivery to moving loads, such as road-way vehicle charging [10], [11], in-motion medical implants [12], [13], and automated material handling in factories [14]–[16].

A dynamic WPT (DWPT) system for industrial automation scenarios is of particular focus in this article. As conceptualized in Fig. 1, it is envisioned to deploy batteryless autonomous moving bases as a replacement of a conventional conveyor within a local manufacturing station to transport items to machines to carry out production tasks. Due to independent direction and speed control of each moving base, the bottleneck imposed by one-way pipelining conveyors (in linear or loop track) can be avoided, and a reconfiguration to streamline the production flow can be greatly simplified. With the benefits of no recharging, simple maintenance, and lower overall cost, the batteryless moving bases are wirelessly powered by means of the transmitter (Tx) coils installed underneath the guided tracks, to the receiver (Rx) coil of the base. Nevertheless, replacing batteries by means of a wireless power source invariably requires a DWPT system that can generate continuous and sufficient magnetic fields at all positions along the track.

One straightforward approach to implement a DWPT for moving loads is to make use of a single large or long Tx coil with one Tx power source to cover the whole track area [14]. However, due to a considerable difference in the sizes of the stationary Tx and moving Rx coils, such a system exhibits high coupling leakage and thus suffers from very low coupling efficiency [15]. Furthermore, the field emission from a larger coil can extend to a longer distance, causing more interference to other electronic devices and incurring higher system sensitivity to nearby metallic objects.

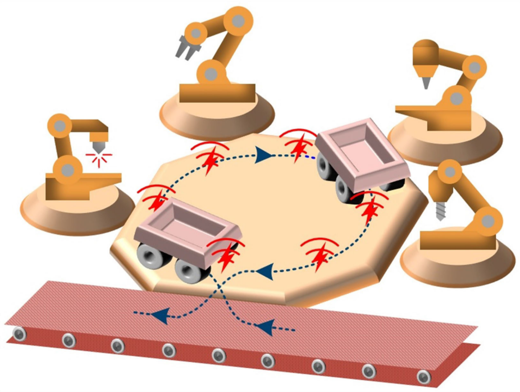

Fig. 1. Conceptual illustration of a DWPT system to power moving bases (after being carried to a manufacturing station by traditional belt conveyor) for local transportation of production items to station's machines, e.g., laser and dispensing. Benefits include independent mobility and control of the bases, as well as ease of reconfiguration.

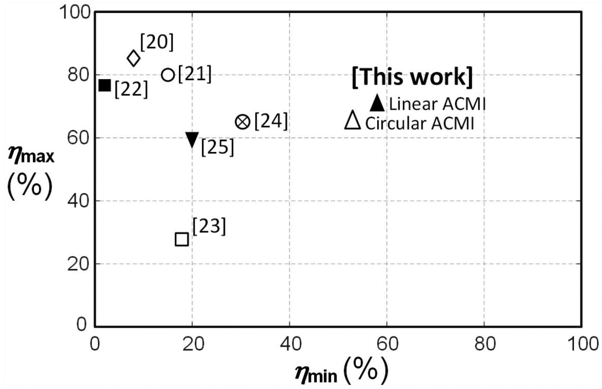

Fig. 2. Plot of maximum versus minimum efficiencies, i.e., $\eta_{\max,\ \min}$, under one Rx and fixed operating frequency conditions for DWPT based on MI waveguides reported in [20]–[25], and ACMI waveguides proposed in this work. Efficiency values toward 100% (top right corner of the plot) indicate better performance.

To resolve this issue, a segmentation into parallel-connected Tx coils equipped with arrays of Tx sources can be used [15], [17], [18]. To obtain further improvement on power efficiency, the segmentation using series-connected Tx coils with Rx-position-dependent activation of distributed Tx arrays can be employed [16], [19]. However, due to the need for multiple Tx coils with multiple power sources, these segmented configurations inevitably entail high implementation complexity and cost.

With the potential benefits of lower cost and complexity, the magnetoinductive (MI) waveguide formed by a periodic array (in one, two, or three dimensions) of coupled resonant coils that hosts the MI wave (MIW) propagation hold promise for the DWPT system of Fig. 1 with a single Tx source and free-positioned moving Rx loads [20]–[26]. It should be pointed out that although the domino coil arrangement shares a similar structure to the one-dimensional (1-D) MI waveguide, its intermediate coils only serve as a relay for end-to-end power transfer between stationary Tx source and Rx load [27]–[29]. Accordingly, only the transfer characteristics between the two ends were studied, normally through traditional circuit analysis. On the other hand, for the MI waveguide, Tx power is transferred to the moving load via magnetic coupling between the Rx coil and any of its cascaded coils. Due to the operation with multiple Rx locations, a more suitable analysis based on the MIW characteristics was introduced [23]. Because the MI waveguide can be expanded indefinitely to cover a wider area, it is also different from the traditional multicoil structures, which eliminate mutual coupling fluctuation between stationary Tx and limited-motion Rx coils over a specific area through a fixed number and specific design or arrangement of Tx coils [9], [10].

One major challenge concerning the use of the MI waveguide for DWPT is the adverse impact of standing waves due to interferences among the propagating MIWs that cause both power null and low power transfer efficiency at periodic Rx locations. Fig. 2 is a summary plot of the minimum versus maximum efficiencies along the MI waveguides reported in the literature under one Rx and fixed operating frequency conditions. It is seen that, with the conventional MI structure in [21] and [22], although the maximum efficiency could reach up to 90%, the minimum value was as low as a few percent (see "○ [21]" and "■ [22]" in Fig. 2). Although the periodic nulls were removed under a matched termination in the waveguide, the overall efficiency become quite low (see "□ [23]"). To alleviate the limitation, various methods were developed based on automatic adjustment of the resonator(s) at or near the termination to relocate power nulls for a different Rx location [20], [24], [25]. By shifting the self-resonant frequency of the terminating resonator, the extent of power nulling zones was reduced, albeit not entirely removed (see "◇ [20]"). Through the theoretical analysis based on the physics of MIWs [23], [24], a switchable termination between low and high impedance was introduced at the last resonator to address power nulling and low efficiency (see "⊗ [24]" in Fig. 2). An automatic scheme for modulating the terminating impedances of the last two resonators in combination with an off-resonance operation was then developed to shift power nulls away from the Rx location in real time (see "▼ [25]"). It is noted that these methods require additional control circuitry with direct/indirect detection of the Rx location. Moreover, as evident from the plot of Fig. 2, further improvement in the overall efficiency is still necessary.

In this article, a true nulls-free 1-D MI waveguide employing alternate coupling polarities between the cascaded resonators is proposed as a basis for the batteryless DWPT system of Fig. 1. The alternate coupling principle is envisaged by virtue of a theoretical extension of the MIW analysis in [23], which enables more explicit and concurrent characterization of the MI waveguide in a generalized manner. In particular, two configurations of the alternately coupled MI (ACMI) waveguide are developed—one with a quadrature-phase impedance termination, and the other with a circular structure suitable for the DWPT implementation. Based on theoretical investigation via the extended analysis, practical validation via measured characterization, and an experimental model of the DWPT system of Fig. 1, the proposed MI configurations are demonstrated to inherently accomplish nulls-free power transfer from a single Tx to free-positioned Rx's without any requirement of additional control or detection circuitry. As also shown in the plot of Fig. 2(see "▲" and "△"), improvement in the overall efficiency from the linear and circular ACMI configurations is evident.

In Section II, the MIW characteristic is overviewed and the theoretical extension of the 1-D MIW analysis in [23] is formulated for a generalized MI waveguide. In Section III, the DWPT using the conventional MI waveguide is reexamined based on the extended analysis under lossless and single Rx assumptions, to reveal the principal mechanism behind the power nulls. This is followed by the development and theoretical investigation of the linear and circular ACMI waveguide configurations to accomplish true nulls-free dynamic power transfer. In Section IV, the efficiency characteristics with losses are analyzed. Section V provides the implementation and performance of the proposed ACMI waveguides operating at 13.56 MHz in comparison with the theoretical analysis and simulations. Also demonstrated in this section is practical feasibility via an experimental ACMI-based DWPT system with a few Watts power levels. Finally, Section VI concludes this article. For ease of reference, the lists of notation and symbols adopted in this article are summarized in Tables I and V.

II. EXTENDED ANALYSIS OF 1-D MI WAVEGUIDE FOR DYNAMIC WPT

A 1-D MI waveguide is a cascade of identical LC resonators coupled via magnetic linkage between adjacent resonator coils. Mainly used for a DWPT system [31]–[33], the MI waveguide delivers an input power P_{in} from a single Tx source to the load Z_{L} in a free-positioned Rx at an output power P_{out} via magnetic coupling from any of its resonator coils along the waveguide. This is in contrast to the traditional domino coil system, where the intermediate coils serve only as a power relay. For brevity, the 1-D waveguide is also referred to as the MI line, and each of its resonators is referred to as a cell.

Fig. 3(a) shows a circuit schematic of the conventional MI line with a total of N cells, from cell 1 to cell N. Each of the cells is modeled by a self-inductance L, a capacitance C, and a loss resistance R, which account for the total loss in L and C. The Tx cell (cell 1) contains a voltage source V_{S} with a source impedance Z_{S}. The free-positioned Rx cell moving along the line is typically an identical resonator loaded with a series load impedance Z_{L}. Although not shown, additional receivers coupled to other cell locations can be employed. The magnetic coupling between adjacent cells is modeled by a mutual inductance M, and the Rx coupling is modeled by a mutual inductance M_X. It is mainly through the modification of an identical mutual inductance M in the conventional line to mutual inductances with alternate polarities that a true nulls-free MIW-based DWPT is achieved in this article.

A. Modeling of MI Waves

The MI waveguide is known to host a propagation of an MIW [31]–[33], which is in fact the real physical mechanism of power delivery along the line. At cell $n \in [1, N]$, the MIW propagation can be characterized in terms of an incident current wave (I_n^+) traveling toward the termination cell N, and a reflected wave (I_n^-) toward the input cell 1 [cf., Fig. 3(a)]. The representation in form of a complex current wave, i.e., $I_n^{\mp} = u \cdot I_{n\pm1}^{\mp} e^{-\gamma d} = u \cdot I_{n\pm1}^{\mp} e^{-(\alpha d + j\beta d)}$, is adopted here, where the frequency dependence term $e^{j\omega t}$ is assumed. $u = \text{sgn}(M)$ is the polarity of the mutual inductance from cell $n \pm 1$ to cell n, and $\gamma d = \alpha d + j\beta d$ denotes the propagation constant per cell, with the attenuation per cell αd and the phase constant per cell βd. The total loop current at cell n is the sum of its incident and reflected MIWs, i.e., $I_n = I_n^+ + I_n^-$. With reference to Fig. 3(a), the input power from

TABLE I
NOTATION AND SYMBOLS

Symbol	Definition/Explanation
γd	Propagation constant per cell
αd	Attenuation per cell
βd	Phase constant per cell
N	Total number of cells
$n,\ m$	Cell index
$M,\ M_X$	Mutual inductance between adjacent cells, mutual inductance between cell and Rx cell
u_n	Polarity of mutual inductance from cell n to $n+1$
k	Coupling coefficient/factor
X	Positive mutual impedance
L	Self-inductance of resonator cell
C	Capacitance of resonator cell
R	Total loss resistance of resonator cell
Q	Quality factor
Q_d	Normalized quality factor or figure of merit
A_{coil}	Coil area
I_n	Total loop current at cell n
$I_n^+,\ I_n^-$	Incident current wave, reflected current wave
V_n	Induced voltage at cell n
V_{S}	Source voltage
$I_{\text{S}},\ I_{\text{L}}$	Source current, load current
ρ_n	Reflectance at cell n
τ_{n+1}	Transmittance from cell n to cell $n+1$
$Z_{\text{S}},\ Z_{\text{L}}$	Source impedance, load impedance
Z_{eTn}	Effective terminating impedance at any cell n
Z_{Tr1}	Transfer impedance from cell 1
Z_n	Referred impedance at cell n from Rx cell
Z_{in}	Input impedance
Z_{ref}	Reference impedance in measurement
Z_0	Characteristic impedance
R_{L}	Load resistance
R_0	Real characteristic impedance under lossless conditions
P_{avl}	Maximum available power
$P_{\text{in}},\ P_{\text{out}}$	Input power, output power
δ	Multiplying factor to exclude Rx loss in P_{out}
$\eta,\ \eta_{avg}$	Power transfer efficiency, average efficiency
$\omega,\ \omega_0$	Angular frequency, resonance frequency
$S,\ \Gamma$	Scattering parameter, reflection coefficient
$\text{W},\ \text{L}$	Width, length of square coil
$\text{R}_{\text{in}},\ \text{R}_{\text{a}}$	Inner radius, width of circular-arc coil
A_{cell}	Sector angle of circular-arc coil
$\text{p}_{\text{d}},\ \text{p}_{\text{a}}$	Overlapping displacement of coupled square coils, overlapping arc of coupled circular-arc coils
$\text{s}_{\text{d}},\ \text{s}_{\text{a}}$	Gap between coupled square coils, circular-arc coils
$\text{g}_{\text{d}},\ \text{g}_{\text{a}}$	Copper trace gap of square coil, circular-arc coil
$\text{w}_{\text{d}},\ \text{w}_{\text{a}}$	Copper trace width of square coil, circular-arc coil

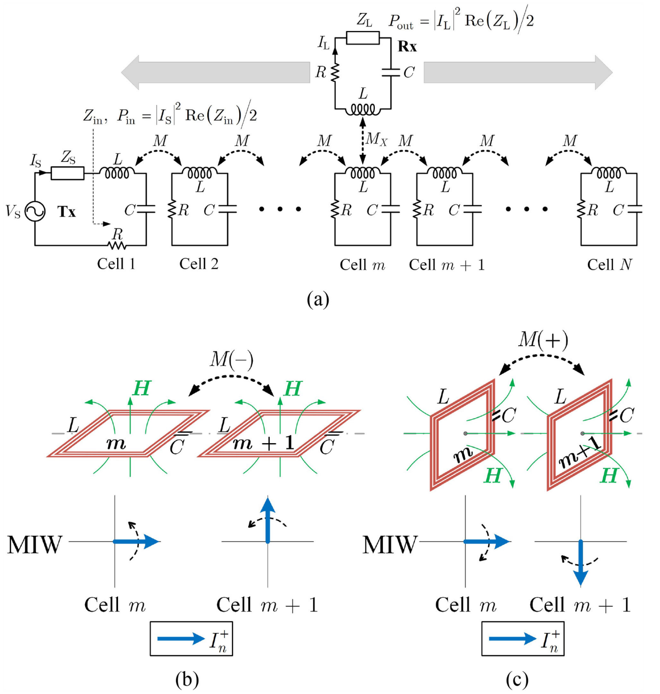

Fig. 3. Conventional 1-D MI line: (a) Typical circuit schematic including transmitter (Tx) and receiver (Rx), along with definitions of input and output power (P_{in} and P_{out}), (b) MI line with coplanar (side-by-side) loop arrangement, and (c) MI line with coaxial (face-to-face) loop arrangement. Rotating phasors of MIWs propagating from left to right are also shown.

the Tx is defined as $P_{\text{in}} = |I_{\text{S}}|^2 \cdot \text{Re}(Z_{\text{in}})/2$ and the output power coupled to the load Z_{L} of the Rx as $P_{\text{out}} = |I_{\text{L}}|^2 \cdot \text{Re}(Z_{\text{L}})/2$, where Z_{in} is the input impedance of the MI line. I_{S} and I_{L} are the source and load currents, respectively.

Under a small loss condition, the attenuation and phase constants per cell can be approximated by [32]

$$\alpha d = \sinh^{-1}(1/2kQ) = \sinh^{-1}(R/2\omega kL) \tag{1a}$$

$$\beta d = \cos^{-1}((\omega_0^2/\omega^2 - 1)/2k) \tag{1b}$$

where $\omega_0 = 1/\sqrt{LC}$ denotes the resonance frequency of each cell, $Q = \omega_0 L/R$ denotes the quality factor, and $k = M/L$ is the mutual coupling factor between adjacent cells. From (1a), under a lossless condition ($R = 0$), we have $\alpha d = 0$ and the MIW propagates with a constant amplitude. Under a lossy condition $(R > 0)$, $\alpha d > 0$ and this yields an amplitude attenuation in the MIW propagation. From (1b), we also have $\beta d = \pi/2$ at the resonant frequency ω_0, which is a typically operating frequency of the MI line for DWPT applications.

The polarity u of the mutual inductance M, or equivalently of the coupling factor k, between two coupled-resonator coils is determined by the relative direction of the flux linkage crossing through the coil surfaces. For the sake of description, consider typical coupled coils with side-by-side and coaxial orientations in Fig. 3(b) and (c), respectively. By invoking Lenz's law, the opposite flux linkage direction in the side-by-side coils results in $u = -1$. Therefore, due to the term $u \cdot e^{-\gamma d}$ in the complex wave representation at the resonant frequency, the propagating MIW exhibits phase progression at $+\pi/2$ rad as illustrated by the rotating phasors in Fig. 3(b). For the coaxial coils in Fig. 3(c), the flux direction is the same, yielding $u = +1$ and phase progression at $-\pi/2$ rad as shown by the propagating MIW phasors in the figure.

With reference to Fig. 3(a), the MI line is under a matched condition when the Rx is coupled to the last cell (cell N) and yields a referred series impedance $Z_{\text{N}} = Z_0 = j\omega M e^{-\gamma d}$ [33], where Z_0 is akin to the characteristic impedance of a waveguide, and exhibits only a real value $Z_0 = \omega_0 M e^{-\alpha d} = R_0$ at ω_0. Under the condition, the incident MIW propagates with no reflection from the Tx at cell 1 toward the termination at cell N, delivering the maximum available power, P_{avl}, to the Rx load Z_{L}. On the other hand, when the Rx coil is coupled to cell m $(m < N)$ before the last cell, a discontinuity is introduced even if it yields the same referred series impedance $Z_m = Z_0$. As a result, the MIW undergoes both reflection and transmission at cell m.

B. Extended Analysis Formulation of the Generalized 1-D MI Line and Beyond

In [23], the theoretical analysis of the MI line for DWPT was elegantly developed via the relation between the effective terminating impedance Z_{eT} and the reflectance ρ, defined as the ratio between the reflected and incident MIWs in a resonator cell. However, the need for successive conversions between Z_{eT} and ρ from cell N back to cell 1 makes the analytical results less explicit. It is also unclear whether the analysis method is amenable to analyzing an MI line beyond one dimension, as in the case of the circular MI structure proposed in this work.

Developed in this section is an extended analytical treatment of the 1-D MI line, which includes not only the reflectance ρ but also the transmittance τ, defined as the ratio between the transmitted and incident MIWs. The inclusion of the transmittance enables more straightforward and concurrent analysis than the use of only the reflectance in [23]. This extended analysis is also applicable to a MI waveguide structure beyond one dimension.

By modeling the effect of the coupled receiver at cell n (for $n \in [1, N]$) via a referred series impedance Z_n as shown in Fig. 4(a), the analysis model of the generalized MI line is given in Fig. 4(b). Note that an additional (reactive) impedance at cell n can also be included in Z_n. Instead of employing only identical mutual inductance M (or coupling factor k) as in the schematic of the conventional line in Fig. 3(a), the model incorporates different mutual coupling polarities between adjacent resonator cells. It is this additional design freedom on the coupling polarity that is crucial to accomplishing a true nulls-free MI waveguide for DWPT. For ease of analysis formulation, the polarity is explicitly shown by the parameter $u_n = \pm 1$. Together with the positive mutual impedance X defined as, $X = j\omega|M| = j\omega|k|L > 0$, the mutual impedance between cell n and $n+1$ is $u_n X$. From [23], the referred impedance Z_n due to the coupling of the Rx load impedance Z_{L} [see Fig. 4(a)] to the nth cell of the generalized MI model is given by

$$Z_n = (M_X/M)^2 |X|^2 \Big/ (Z + Z_L) \tag{2}$$

where $Z = R + j\omega L + 1/j\omega C$ is the intrinsic series impedance of each resonator cell and $Z = R$ under the resonance operation at ω_0. Also indicated at each cell are the expressions of the incident and reflected waves, I_n^+ and I_n^-, in terms of the reflectance

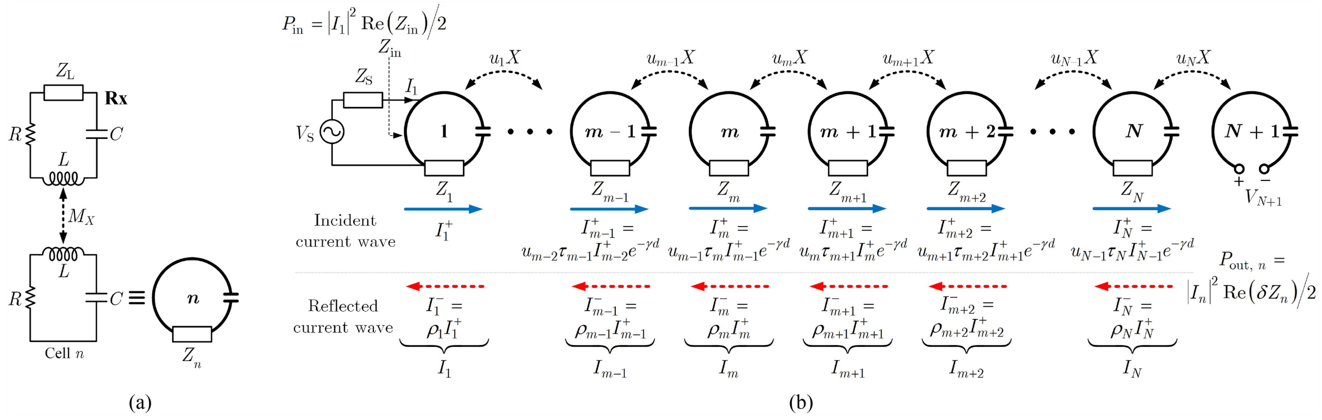

Fig. 4. (a) Resonator cell n coupled to load Z_L at Rx cell and symbol representation with referred impedance Z_n.(b) Analysis model of generalized MI line with cell 1 to cell N loaded by an impedance Z_n. Additional open-circuit cell $N+1$ is included for analysis extension beyond one dimension. Also indicated are expressions for incident (→) and reflected (⇢) MIWs, as well as input power (P_{in}) and output power at cell n ($P_{\mathrm{out},n}$).

$\rho_n = I_n^-/I_n^+$ and transmittance $\tau_{n+1} = |I_{n+1}^+/I_n^+|$.The model also includes an additional open-circuit cell $N+1$ for expanding the analysis to an MI waveguide structure beyond one dimension.

Let us consider a section of the 1-D MI line comprising cell $m-1$ up to cell $m+2$ in Fig. 4(b). To study how the MIW is reflected and transmitted at the discontinuity due to Z_m at cell m, we set $Z_{m-1} = Z_{m+1} = Z_{m+2} = 0$. The result from this simplification will be expanded to an arbitrary case with nonzero Z_n at any cell n in Section IV-A. By applying Kirchoff's voltage law, the recurrence equations in terms of the self-loop and coupled-loop currents at steady state governing the resonator cells m and $m+1$, respectively, are given by

$$(Z + Z_m)\, I_m + u_{m-1}XI_{m-1} + u_mXI_{m+1} = 0 \quad (3)$$

$$ZI_{m+1} + u_mXI_m + u_{m+1}XI_{m+2} = 0. \quad (4)$$

For the cells with $Z_n = 0$, we have $\rho_n = \rho_{n+1}\cdot e^{-2\gamma d}$ and $\tau_{n+1} = +1$. Following this, the total loop currents of the line section around cell m are given with reference to I_m^+ by

$$I_{m-1} = u_{m-1}I_m^+(e^{+\gamma d} + \rho_m e^{-\gamma d}) \quad (5a)$$

$$I_m = I_m^+(1 + \rho_m) \quad (5b)$$

$$I_{m+1} = u_m\tau_{m+1}I_m^+e^{-\gamma d}(1 + \rho_{m+1}) \quad (5c)$$

$$I_{m+2} = u_{m+1}u_m\tau_{m+1}I_m^+e^{-2\gamma d}(1 + \rho_{m+1}e^{+2\gamma d}). \quad (5d)$$

Note that the transmittance τ_{m+1} and the reflectance ρ_m are due to Z_m, whereas ρ_{m+1} is due to the reflection beyond cell $m+2$. By using (5b), the output power $P_{\mathrm{out},m}$ delivered to the load Z_L of the coupled Rx at cell m can be determined from the referred impedance Z_m given in (2) by

$$P_{\mathrm{out},m} = |I_m|^2 \cdot \mathrm{Re}\,(\delta Z_m)\Big/2 \quad (6)$$

where the resonator losses in the Rx is excluded by the factor $\delta = \mathrm{Re}(Z_L)/(R + \mathrm{Re}(Z_L))$. The set of equations (2)–(6) are central to the MI waveguide analysis in Section III under lossless conditions and Section IV-B under lossy conditions.

III. Nulls-Free ACMI-Based Dynamic WPT

In this section, the extended analysis formulated in Section II-B is employed to investigate the nulling effect caused by standing waves in the conventional MI line for DWPT. With the insight gained on the destructive interference mechanism between the incident and reflected MIWs, the MI line configurations using the alternate coupling polarity that inherently remove the power nulls are then presented.

To facilitate the investigation without loss of generality, the following assumptions are applied to the generalized MI model of Fig. 4(b) to obtain closed-form expressions at the resonance operation, including a lossless line, a matched referred impedance at cell m ($Z_m = R_0$), a reactive impedance termination Z_N, and $Z_n = 0$ at $n \neq m$ and N. Note that in Section IV, the MI lines with losses and series impedances at any cell will be analyzed to enable characterization of the power transfer efficiency and validation of the analysis integrity with simulation and measurement.

A. Closed-Form Equations for Lossless 1-D MI Line With Single Load and Termination

By using (1), the lossless condition yields the attenuation constant per cell $\alpha d = 0$ and the phase factor per cell $\beta d = \pi/2$. Thus, we have $e^{\pm\gamma d} = e^{\pm j\pi/2} = \pm j$ in the complex MIW representation, and the characteristic impedance is real, i.e., $Z_0 = -jX = R_0 = \omega_0 M$. With the use of (5), the total loop currents of the line section around cell m can be given with reference to I_m^+as $I_{m-1} = ju_{m-1}I_m^+(1-\rho_m)$, $I_m = I_m^+(1+\rho_m)$, $I_{m+1} = -ju_m\tau_{m+1}I_m^+(1+\rho_{m+1})$, and $I_{m+2} = -u_{m+1}u_m\tau_{m+1}I_m^+(1-\rho_{m+1})$. By substituting these current expressions into (3) and (4) at $Z = 0$, the reflectance ρ_m at cell m can be derived as

$$\rho_m = -\frac{(1-\rho_{m+1})\,Z_m + 2\rho_{m+1}R_0}{(1-\rho_{m+1})\,Z_m + 2R_0} \quad (7a)$$

and the transmittance τ_{m+1} from cells m to $m+1$ as

$$\tau_{m+1} = \frac{(1+\rho_m)}{(1-\rho_{m+1})}. \quad (7b)$$

TABLE II
Closed-Form Expressions of Effective Terminating Impedance and Transimpedance for Lossless 1-D MI Line With Single-Load Impedance $Z_m = R_0$, and Reflectance at Termination ρ_N With $u_{Tr} = \prod_{i=1}^{N} u_i$

N	m	Z_{eT1}	Z_{Tr1}
Odd	Odd	$\frac{2}{1+\rho_N}\cdot R_0$	$-\frac{u_{Tr}R_0}{j^N}$
	Even	$\frac{1-\rho_N}{2}\cdot R_0$	$-\frac{1+\rho_N}{2}\cdot\frac{u_{Tr}R_0}{j^N}$
Even	Odd	$\frac{2}{1-\rho_N}\cdot R_0$	$-\frac{1+\rho_N}{1-\rho_N}\cdot\frac{u_{Tr}R_0}{j^N}$
	Even	$\frac{1+\rho_N}{2}\cdot R_0$	$-\frac{1+\rho_N}{2}\cdot\frac{u_{Tr}R_0}{j^N}$

TABLE III
Closed-Form Expressions for Input Impedance Z_{in} and Load Power $P_{\text{out},m}$ for the Conventional MI Line

N	m	Z_{in}		$P_{\text{out},m}$	
		$Z_N=0$	$Z_N=\infty$	$Z_N=0$	$Z_N=\infty$
Odd	Odd	R_0	∞	P_{avl}	0
	Even	0	R_0	0	P_{avl}
Even	Odd	∞	R_0	0	P_{avl}
	Even	R_0	0	P_{avl}	0

When cell $m = N$, we have $I_{N+1} = 0$ and thus $\rho_{N+1} = +1$. By using (7a), the reflectance at the termination of the generalized MI line of Fig. 4(b) is

$$\rho_N = -\frac{(Z_N - R_0)}{(Z_N + R_0)}. \tag{8}$$

Since $Z_n = 0$ for $m + 1 \le n \le N - 1$, we have $\rho_n = -\rho_{n+1}$, $\tau_{n+1} = +1$ and, thus, $\rho_{m+1} = -\rho_n(-1)^{N-m}$. Substituting this into (7) and using the expression in Fig. 4(b), the incident and reflected MIW currents at cells 1 to N under the matched single load $Z_m = R_0$ and the termination Z_N are derived as

$$I_n^+ = \begin{cases} j^{-(n-1)} \prod_{i=1}^{n} u_{i-1}, & 1 \le n \le m \quad (9a) \\ \tau_{m+1} j^{-(n-1)} \prod_{i=1}^{n} u_{i-1}, & m+1 \le n \le N \quad (9b) \end{cases}$$

$$I_n^- = \begin{cases} \rho_m I_n^+, & 1 \le n \le m \quad (10a) \\ \rho_N (-1)^{N-n} I_n^+, & m+1 \le n \le N \quad (10b) \end{cases}$$

where $\rho_m = -(1 - \rho_N(-1)^{N-m})/(3 + \rho_N(-1)^{N-m})$ and $\tau_{m+1} = 2/(3 + \rho_N(-1)^{N-m})$ with ρ_N given by (8). Based on (7)–(10), the closed-form expressions for the effective terminating impedance at cell 1 (Z_{eT1}) can be derived. Also derived for an analysis of the MI line beyond one dimension is the transfer impedance Z_{Tr1}, defined as the ratio between the coupled voltage to cell $N + 1$ (with $Z_{N+1} = \infty$) and the loop current at the input cell 1, i.e., $Z_{Tr1} = V_{N+1}/I_1 = u_N X I_N/I_1$. Table II summarizes Z_{eT1} and Z_{Tr1} versus even and odd number types of the Rx cell location m, and the total number of cells N.

Under the lossless assumption, the power $P_{\text{out},m}$ delivered to the referred Rx load impedance $Z_m = R_0$ is exactly equal to the Tx power P_{in} to the input of the MI line, i.e., the efficiency $\eta = P_{\text{out},m}/P_{\text{in}} = 1$. Note that $P_{\text{out},m}$ can be calculated using (6) with $\delta = 1$. The closed-form equations in this section are employed to study the lossless MI lines as discussed next.

B. Power Nulls in Conventional MI Line Revisited

The conventional MI line for DWPT is implemented using identical coupling polarity factors $u_n = +1$ or -1 for $n =$ 1 to N. To address the power nulling issue in [23], a simple means is to make the termination switchable between short and open impedance, $Z_N = 0$ and $Z_N = \infty$, respectively. Thus, to investigate the mechanism that leads to the power nulling, we consider the conventional line under both termination impedances. To simplify the explanation, all the polarity factors are chosen positive, $u_n = +1$, which yields a clockwise (CW) phase progression in the propagating MIWs similar to electromagnetic waves propagation in a typical waveguide.

Let us consider the MI line with no receiver. By using (8), we have $\rho_N = +1$ at $Z_N = 0$, and $\rho_N = -1$ at $Z_N = \infty$. Based on (9) and (10), we have $\rho_m = \rho_N (-1)^{N-m}$ and $\tau_{m+1} = +1$ at $Z_m = 0$ with $m \in [1,\ N - 1]$, and the incident/reflected MIWs for the last three cells of the line with normalization to the incident wave are shown in Fig. 5(a) in the form of phasor representation. In the figure, the incident MIW propagates with a CW phase progression per cell at $\beta d = \pi/2$ toward cell N, where it undergoes a total in-phase reflection under a short termination $Z_N = 0$, and an out-of-phase reflection under an open termination $Z_N = \infty$. As the reflected MIW I_n^- propagates back toward the source with the same phase progression, it interferes with the incident MIW I_n^+ creating standing waves that exhibit both total summation and total cancellation or nulling of the loop currents I_n. Note from the figure that the destructive standing wave patterns are opposite under the short and open terminations. Consequently, the source power can be delivered to the load only when the receiver is coupled to the cells with nonzero loop current.

Consider the case with the receiver coupled to cell $m = N - 2$. By using (8)–(10), we have $\rho_{N-2} = 0$ and $\tau_{N-1} = +0.5$ at $Z_N = 0$, whereas $\rho_{N-2} = -1$ and $\tau_{N-1} = +1$ at $Z_N = \infty$. Subsequently, the normalized MIWs of the last three cells are shown in Fig. 5(b). Under the short termination, the loop current at the coupled receiver cell $N - 2$ is equal to the incident MIW, and hence the source power is delivered to the load. Note that after the cell, the magnitude of the transmitted and reflected MIWs is reduced by half. On the contrary, the open termination results in nulling of the loop current at cell $N - 2$, and hence no power is delivered to the load. For the MI line implemented by the square coils with side-by-side couplings for $u_n = -1$ [see Fig. 12(a)], the simulated magnetic field distribution using an EM simulator is depicted in Fig. 5(c), where the nulling of the coupled field from cell $N - 2$ to the Rx coil with a load is evident.

With the use of the expressions in Table II, the input impedance $Z_{\text{in}} = Z_{eT1}$ of the conventional MI line versus the Rx cell location m and the total cells N are summarized in Table III,

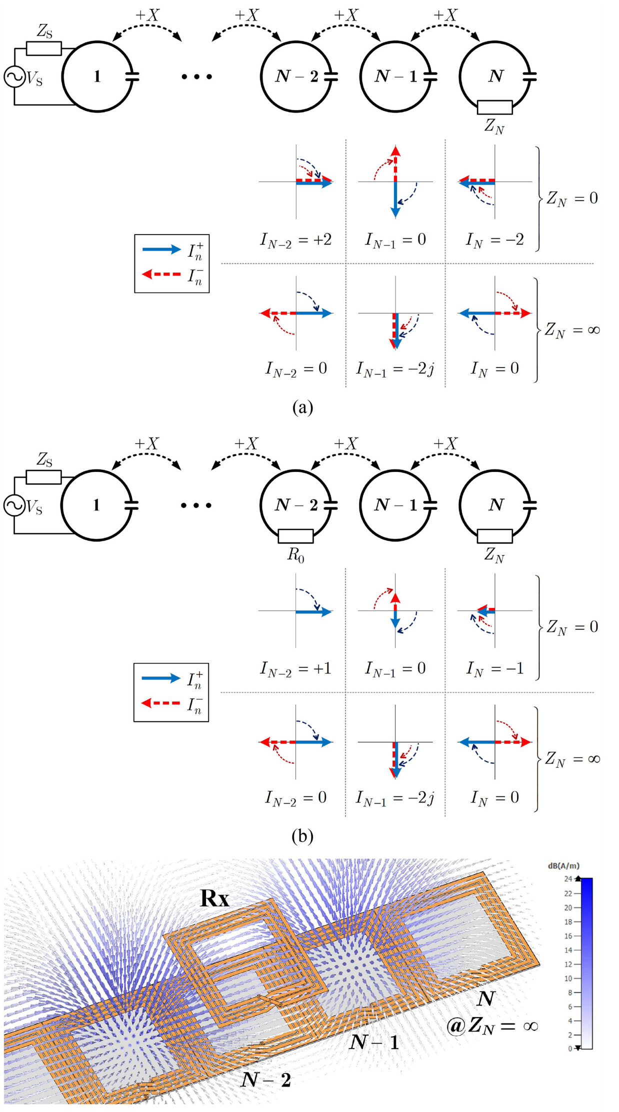

(a)

(b)

(c)

Fig. 5. Phasor representation of (incident → /reflected ⇢) MIWs and loop currents of the conventional MI line under open and short terminations, for the case of (a) no receiver and (b) receiver coupled to cell $N-2$. Depicted in (c) is simulated magnetic field distribution at Rx cell coupled to cell $N-2$ of the conventional line implemented using square coils under open termination.

under the terminations $Z_N = 0$ and $Z_N = \infty$. Also given in the table is the corresponding load power $P_{\mathrm{out},m}$ determined using (6). Note that $P_{\mathrm{avl}} = V_{\mathrm{S}}^2/8R_0$ is the maximum available power under the input matched condition, i.e., $Z_{\mathrm{S}} = Z_{\mathrm{in}}^*$, where the asterisk denotes the conjugate operator. When $Z_{\mathrm{in}} = R_0$, we have $P_{\mathrm{out},m} = P_{\mathrm{avl}}$, and when $Z_{\mathrm{in}} = 0$ or ∞, we have $P_{\mathrm{out},m} = 0$. As evident in the table is the periodic characteristic with the Rx location m for both the input impedance (between $Z_{\mathrm{in}} = 0$, ∞, and R_0), and the load power (between $P_{\mathrm{out},m} = 0$ and P_{avl}). In particular, under $Z_N = 0$, we obtain $Z_{\mathrm{in}} = R_0$ and $P_{\mathrm{out},m} = P_{\mathrm{avl}}$ when the receiver is coupled to cell m, with m being the same odd or even number type as the total cells N. On the other hand, under $Z_N = \infty$, the same are obtained when m is of the opposite type to N. Such characteristics are in line with the observation in Fig. 5(a) and (b) and [23].

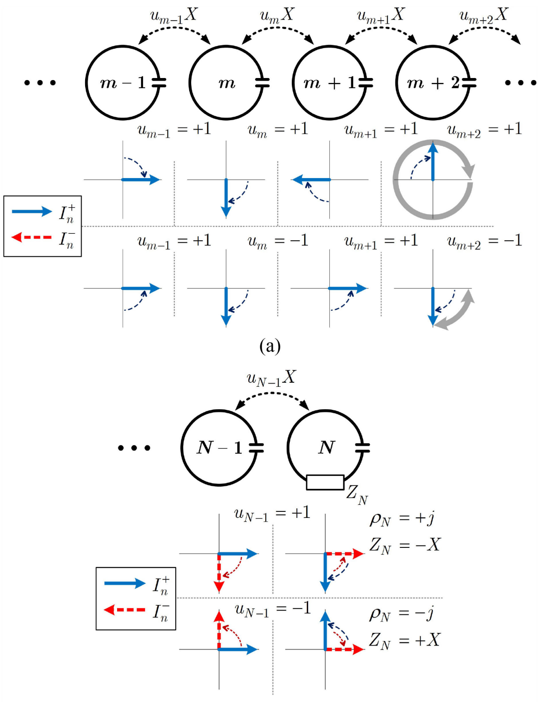

(a)

(b)

Fig. 6. (a) Generalized MI line section with corresponding phasor rotations of MIW (for the left to right propagation) under uniform and alternate coupling polarities between successive resonator cells. (b) Quadrature-phase terminations at cell N for alternate phase change between incident (→) and reflected (⇢) MIWs, and their corresponding phasor rotations.

C. ACMI Waveguide and Its Operation

From the above theoretical investigation of the conventional MI line for DWPT, it can be deduced that the power transfer nulls caused by standing waves are attributed to the changing of phase associated with the propagation of MIWs along the line and the reflection at the termination. In fact, such a destructive interference mechanism is inevitable in any form of waveguides whereby two oppositely propagating waves with the same magnitude become out-of-phase at one point, yielding a total cancellation, and consequent power nulls in the MI line. Nevertheless, it is this seemingly unavoidable characteristic that provides a key basis to overcome the issue of power transfer nulls at minimum cost to complexity. To this end, it is proposed in this work the MI line with alternate mutual coupling polarities that can limit the phase progression of the propagating incident and reflected MIWs.

Let us consider a section of the generalized MI line in Fig. 6(a). Under a uniform coupling polarity where the polarity product between successive couplings is $u_{n-1} \cdot u_n = +1$, the MIW undergoes a constant phase change as it propagates between cells along the line. Based on (9), this allows the phase progression of the MIW to revolve over a complete cycle (2π rad), as depicted in Fig. 6(a) by the CW rotation of its phasor representation for the case of $u_{m-1} = u_m = u_{m+1} = u_{m+2} = +1$.

To accomplish a limit on the amount of phase progression of the propagating MIW, the coupled resonator cells are incorporated with alternate coupling polarities, where the polarity

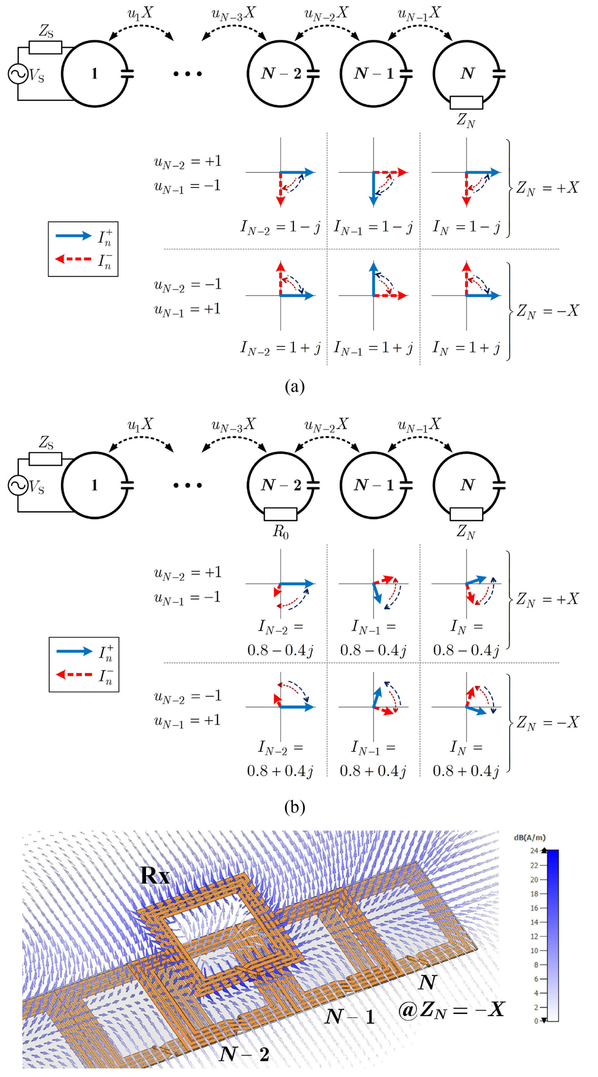

(a)

(b)

(c)

Fig. 7. Normalized MIWs and loop current along the ACMI line under $Z_N = \pm X$ for the case of (a) no receiver and (b) receiver located at cell $N-2$. Depicted in (c) is simulated magnetic field distribution with Rx cell coupled to cell $N-2$ of the ACMI line implemented using square coils under $Z_N = -X$.

TABLE IV

CLOSED-FORM EXPRESSIONS FOR INPUT IMPEDANCE Z_{in} AND LOAD POWER $P_{\text{out},m}$ FOR THE ACMI LINE WITH QUADRATURE PHASE TERMINATION $Z_N = \pm X$

N	m	Z_{in}		$P_{\text{out},\,m}$	
		$Z_N=+X$	$Z_N=-X$	$Z_N=+X$	$Z_N=-X$
Odd	Odd	$(1+j)\cdot R_0$	$(1-j)\cdot R_0$	$0.8P_{\text{avl}}$	$0.8P_{\text{avl}}$
	Even	$(1+j)\cdot R_0/2$	$(1-j)\cdot R_0/2$		
Even	Odd	$(1-j)\cdot R_0$	$(1+j)\cdot R_0$	$0.8P_{\text{avl}}$	$0.8P_{\text{avl}}$
	Even	$(1-j)\cdot R_0/2$	$(1+j)\cdot R_0/2$		

product between successive couplings is $u_{n-1} \cdot u_n = -1$. This can be shown by the section of the generalized MI line of Fig. 6(a) with $u_{m-1} = u_{m+1} = +1$ and $u_m = u_{m+2} = -1$. In operation, as the MIW propagates from cell $m-1$ to cell m, it undergoes a phase change at $-\pi/2$ rad because $u_{m-1} = +1$, With the subsequent opposite coupling polarity $u_m = -u_{m-1} = -1$, further propagation of the MIW from cell m to cell $m+1$ yields an opposite phase change at $+\pi/2$ rad, thereby restoring the original phase at cell $m-1$. Such a phase restoration operation is repeated as the MIW propagates to subsequent pairs of cells. In effect, the phase progression of the MIW propagating along the ACMI line is confined to revolve over only a quarter of a cycle ($\pi/2$ rad), as shown by its corresponding phasor rotations in Fig. 6(a).

Based upon the alternate coupling principle, two configurations of the ACMI lines for DWPT are developed. One of the configurations incorporates quadrature-phase reflection at the termination, derived from the perspective of alternate coupling polarities. The other makes use of a circular line structure to enable two optional routes on the ACMI line that take turns to transfer power from the Tx to the Rx load.

D. ACMI Line With Quadrature Phase Termination

In the linear conventional MI structure, a lossless reactive termination causes reflection and subsequent cancellation between the incident and reflected MIWs. Since the reflected MIW is essentially the incident MIW that changes its propagating direction at the termination, the concept of the alternate coupling polarities can also be expanded to the selection of the termination impedance Z_N of the linear ACMI line for DWPT.

To keep the relative phase between the two MIWs to within $\pm\pi/2$ rad, the phase change due to the reflection at the last cell N must be in quadrature and opposite (or alternate) polarity to the phase change due to the coupling from the previous cell $N-1$. This is illustrated in Fig. 6(b). For a positive coupling $u_{N-1} = +1$ from cell $N-1$ to cell N, it results in a CW or a negative phase change at $-\pi/2$ rad in the incident MIW. To obtain the alternate phase change at $+\pi/2$ rad in the reflected MIW, the reflectance must be of positive quadrature phase at $+\pi/2$ rad. This consequently yields $\rho_N = +j$, and by using (8), we have the required termination impedance $Z_N = -X$. Conversely, for a negative coupling from the previous cell $u_{N-1} = -1$, which yields a counter CW phase change at $+\pi/2$ rad in the incident MIW, $\rho_N = -j$ must be selected to obtain the reflected MIW with the alternate phase change at $-\pi/2$ rad as also illustrated in Fig. 6(b). In this case, the required termination impedance is $Z_N = +X$. Since Z_N is still of a reactive type, it incurs practically no loss to the linear ACMI line. Note that, in a practical implementation, the required termination impedance can be absorbed in the self-capacitive impedance of the last resonator cell so that only one capacitor can be employed. It is also important to point out that the use of the quadrature-phase termination in the conventional MI line only shifts power transfer nulls to half-point locations between centers of adjacent cells.

Let us consider the ACMI lines with quadrature phase termination for the case of no receiver. Based on (8)–(10), the normalized incident and reflected MIWs for the last three cells are shown in Fig. 7(a) with $Z_N = +X$ and $Z_N = -X$. Under both terminations, the MIWs in each cell are in quadrature phase,

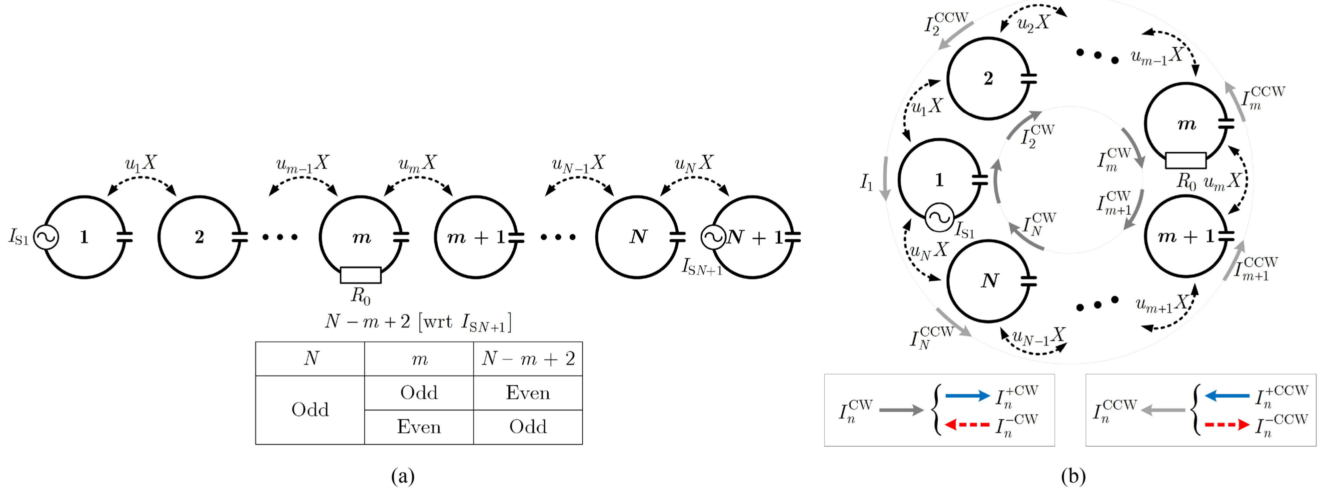

N	m	$N-m+2$
Odd	Odd	Even
	Even	Odd

(a) (b)

Fig. 8. Analysis models of (a) two transmitters located at opposite ends of the ACMI line with $N+1$ cells and (b) circular ACMI line with an odd total cell number N.

and undergo a phase change within $\pm\pi/2$ rad. In addition, *all* the normalized loop currents are in-phase and of equal magnitude, yielding no power nulls at any Rx location.

Consider the case of the receiver coupled to cell $m = N-2$. By using (9) and (10), we have $\rho_{N-2} = 0.2 + 0.4j$ and $\tau_{N-1} = 0.6 - 0.2j$ at $Z_N = +X$, whereas $\rho_{N-2} = -0.2 + 0.4j$ and $\tau_{N-1} = 0.6 + 0.2j$ at $Z_N = -X$. Subsequently, the normalized MIWs and loop currents for the last three cells are shown in Fig. 7(b). It is clear that under both terminations, no cancellation of the MIWs and thus no power transfer nulling is observed at any cell, albeit with nonzero reflectance and hence the transfer of power less than P_{avl}. For the linear ACMI line implemented by the side-by-side/overlapped square coils for $u_n = \pm 1$ [see Fig. 12(a) and (c)], the simulated magnetic field distribution using an EM simulator is depicted in Fig. 7(c). Clearly, the field along the line is continuous, and the coupled field to the Rx coil at cell N–2 is strong.

Similar to its conventional counterpart, the ACMI line with quadrature phase termination can be characterized by using the closed-form expressions in Table II. Summarized in Table IV are the input impedance and the output load power relative to the available power under $Z_N = -X$ and $Z_N = +X$. As indicated, the nulls effect has been removed, and the power delivered to the load is constant at $P_{\mathrm{out},m} = 0.8 \cdot P_{\mathrm{avl}}$, regardless of the Rx location m and the total cells N. Also indicated is the periodic input impedance characteristic between $Z_{\mathrm{in}} = (1 \pm j)R_0$ and $(1 \pm j)R_0/2$, which still results in a constant output power because, under the lossless conditions, we have

$$P_{\mathrm{out},m} = \frac{V_{\mathrm{S}}^2 \cdot \mathrm{Re}\left((1 \pm j)R_0\right)}{2\left|R_0 + (1 \pm j)R_0\right|^2} = \frac{V_{\mathrm{S}}^2 \cdot \mathrm{Re}\left((1 \pm j)R_0/2\right)}{2\left|R_0 + (1 \pm j)R_0/2\right|^2} = 0.8P_{\mathrm{avl}}. \qquad (11)$$

It is clear from (11) that the lower (higher) input impedance is completely counterbalanced by the associated higher (lower) input current supplied by the source, thereby maintaining the amount of power delivered into the ACMI line and hence to the Rx load.

E. Alternately Coupled Circular MI Line

As conceptually illustrated by the analysis model of Fig. 8(a), the other ACMI configuration to overcome the power transfer nulls makes use of two transmitters located at opposite ends of the ACMI line, i.e., at cell 1 and cell $N+1$. With an odd N, the two transmitters essentially take turns to supply power to the receiver load coupled to cell m along the line. For an even N, the same operation is not feasible and thus will not be discussed.

Without loss of generality, the transmitters are assumed a current source type for ease of description. By virtue of superposition, when considering individually the source I_{S1} or $I_{\mathrm{S}N+1}$, the model of Fig. 8(a) yields the ACMI line with a short termination and the total number of cells N. In particular, when I_{S1} is active, the line is terminated at cell N with $Z_N = 0$, and when $I_{\mathrm{S}N+1}$ is active, the line is terminated at cell 2, with $Z_2 = 0$. Based on Table III, for the line with a short termination and an odd N, the source can only supply power to the receiver coupled to an odd-numbered cell m. Following this, for the ACMI line equipped with the two transmitters, I_{S1} can supply power to the receiver load at an odd-numbered cell $m\,(= 1, 3, \ldots, N)$, whereas $I_{\mathrm{S}N+1}$ can supply to the load at an even-numbered cell $m\,(= 2, 4, \ldots, N-1)$, which is an odd-numbered cell with respect to the source $I_{\mathrm{S}N+1}$. In essence, the two sources interchangeably supply power depending on the Rx location, thereby removing the power transfer nulls.

By combining the two transmitters in the 1st and $(N+1)$th cells into one single cell, the circular ACMI line with an odd total cells N is obtained as shown in Fig. 8(b). With the use of (9) and (10), the loop current in each cell can be determined by separately considering the MIWs due to the source I_{S1} in the CW and CCW directions, as indicated by I_n^{CW} and I_n^{CCW} in the

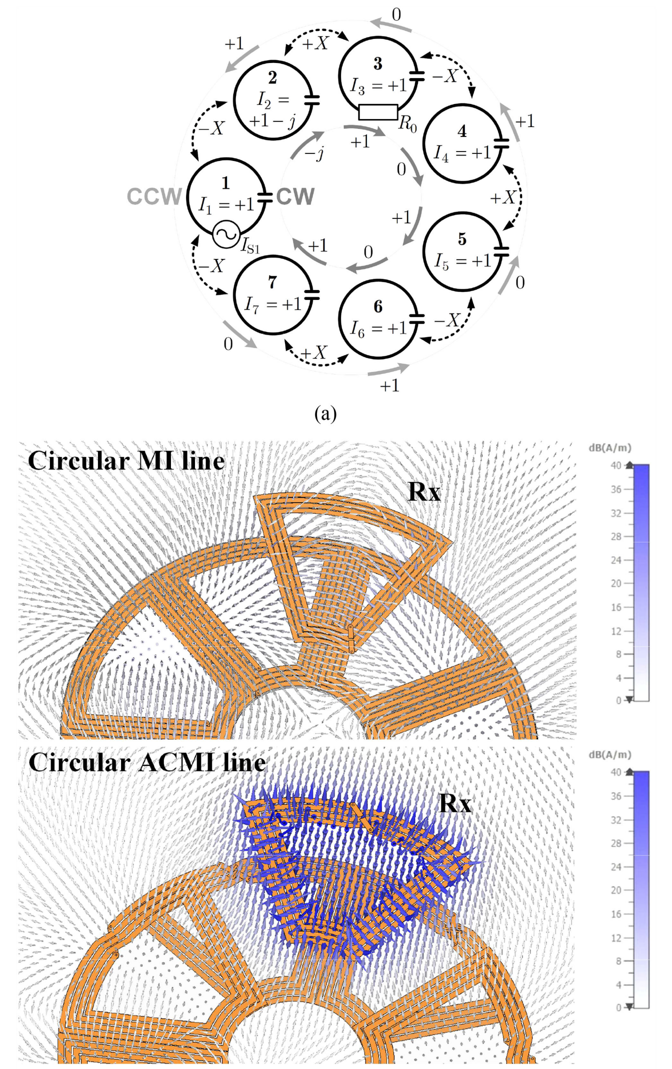

(a)

(b)

Fig. 9. (a) Normalized loop currents in CW and CCW directions of circular ACMI line with $m = 3$ and $N = 7$ and (b) comparison of simulated magnetic field distribution when the Rx cell is coupled to two adjacent cells of the circular MI and ACMI lines implemented using circular-arc coils.

figure. The total loop current I_n in each cell is equal to the sum of the loop currents in both directions, i.e., $I_n = I_n^{\text{CW}} + I_n^{\text{CCW}}$.

Considering the circular line with $m = 3$ and $N = 7$, Fig. 9(a) shows the CW and CCW loop currents normalized to their corresponding $I_1^{+\text{CW}}$and $I_1^{+\text{CCW}}$. Also indicated in the figure are the sum of the normalized currents in each cell. Due to the incorporation of the alternate coupling, the relative phase among the total currents is limited to $\pm\pi/2$ rad. Consequently, when the Rx is located in between two adjacent cells, the Tx power is delivered to the load via the MIW propagation in both the CW and CCW directions. The simulated magnetic field distribution when the Rx cell is coupled to two adjacent cells is depicted in Fig. 9(b) for both the circular MI and ACMI lines implemented using the side-by-side and overlapped coupled circular-arc coil arrangement [see Fig. 12(b) and (d)]. In comparison to its MI counterpart, which exhibits Rx field nulling, the coupled field to the Rx cell of the ACMI line is evident. Note that due to the CW and CCW power transfer paths, which results in nonzero total circulating loop currents in all the cells, the associated loss of the circular line is equivalent to that of two conventional lines.

The input impedance and power transfer characteristics of the circular ACMI line can be examined using the closed-form expressions in Table II. Since cell 1 and cell $N + 1$ in Fig. 8(a) are combined into the Tx cell 1 in Fig. 8(b), which is in turn coupled to both cell 2 and cell N, the input impedance Z_{in} is determined by the sum of the driving-point impedance Z_{eT1} and the transimpedance Z_{Tr1} associated with the MIW propagations from the Tx source in both CW and CCW directions. Based on Table II with $\rho_N = 0$, by combining the impedances Z_{eT1} and Z_{Tr1} resulting from both propagation directions, the net input impedance Z_{in} can be given by

$$Z_{eT1} = \begin{cases} R_0 + 2ju_{Tr}R_0, & N = 1, 5, 9, \ldots \\ R_0 - 2ju_{Tr}R_0, & N = 3, 7, 11, \ldots \end{cases} \tag{12}$$

where u_{Tr} is given in Table II. It is evident from (12) that the nulls-free circular ACMI line exhibits a constant input impedance Z_{in}, independent of the Rx location m. Therefore, with the matched source impedance condition $Z_{\text{S}} = Z_{\text{in}}^*$, the available power P_{avl} from the source to the load can be accomplished.

IV. EFFICIENCY CHARACTERISTICS UNDER LOSSY CONDITIONS

The analytical formulation in Section II-B based on the reflectance and transmittance in the generalized MI line of Fig. 4(b) is now employed with the inclusion of losses and multi-Rx couplings to the resonator cells to derive the incident/reflected MIWs and loop currents, as well as the input/output power and transfer efficiency. Subsequently, the efficiency characteristics of the proposed ACMI lines are investigated in detail. This helps facilitate design implementation of the ACMI lines in a practical scenario, and enables verification of the analysis integrity with simulation and experimentation in Section V.

A. *Analysis With Resonator Losses*

With the substitution of (5) into (3) and (4) at $\alpha d \neq 0$, the reflectance ρ_m and the transmittance τ_{m+1} at cell m of the MI line can be derived as

$$\rho_m = -\frac{\left(e^{+\gamma d} + \rho_{m+1}e^{-\gamma d}\right) Z_m + \left(e^{+\gamma d} - e^{-\gamma d}\right) \rho_{m+1} X e^{-\gamma d}}{\left(e^{+\gamma d} + \rho_{m+1}e^{-\gamma d}\right) Z_m - \left(e^{+\gamma d} - e^{-\gamma d}\right) X e^{+\gamma d}} \tag{13a}$$

$$\tau_{m+1} = \frac{1 + \rho_m}{1 + \rho_{m+1}e^{-2\gamma d}}. \tag{13b}$$

It is noticed from the equations that the factors u_n have no effect on the reflectance and transmittance, and only determine the polarities of the MIWs and loop currents as given in (5).

Based on (13), when $Z_m = 0$, we obtain $\tau_{m+1} = +1$ and $\rho_m = \rho_{m+1}e^{-2\gamma d}$ as expected. For the case that cell m is the last cell and thus Z_m is the terminating impedance, we have the loop current $I_{m+1} = 0$, and thus $\rho_{m+1} = -1$. By using (13a),

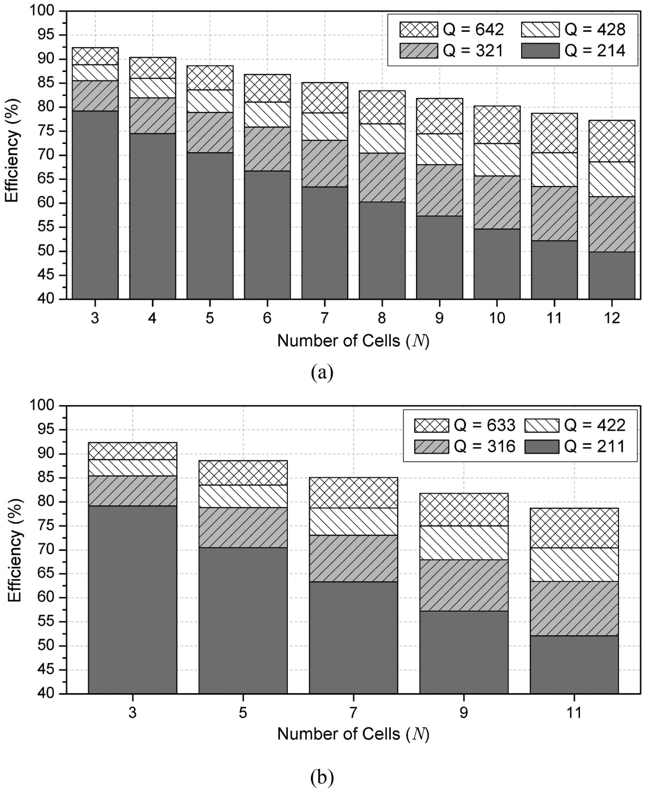

(a)

(b)

Fig. 10. Theoretically calculated average efficiency versus total number of cells for (a) linear ACMI lines and (b) circular ACMI lines (applicable at odd N as described in Section III-E).

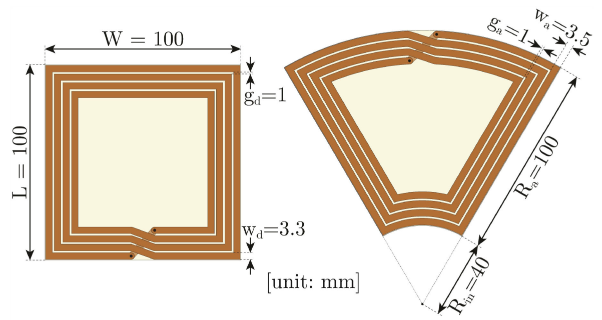

(a) (b)

Fig. 11. Single coil geometry of (a) linear structure and (b) circular structure.

the reflectance at the termination cell becomes

$$\rho_m = -\frac{Z_m - Xe^{-\gamma d}}{Z_m - Xe^{+\gamma d}}. \tag{14}$$

On the other hand, (14) can also be used to determine the effective terminating impedance Z_{eTn} at any cell n along the MI line in terms of its reflectance ρ_n. That is, by rearranging (14), we have

$$Z_{eTn} = X\left(\frac{e^{-\gamma d} + \rho_n e^{+\gamma d}}{1 + \rho_n}\right). \tag{15}$$

The analysis of the MI line starts with recursive calculation of the reflectance ρ_n and the transmittance τ_n from the termination cell $n = N$ toward the input cell $n = 1$. At the last cell N, the reflectance ρ_N is given by (14) with $Z_m = Z_N$, and for the subsequent cell $1 < n < N$, ρ_n is given by (13a) with $m = n$. The transmittance τ_n is then calculated by using (13b). Following this, the MIWs and the corresponding loop currents are determined in terms of the incident current wave I_1^+ at the input cell, from cell $n = 1$ toward the last cell N. With the use of (5b) and (5c), it can be shown that

$$I_n = I_1^+(1+\rho_n)e^{-(n-1)\gamma d}\prod_{i=1}^{n} u_{i-1}\tau_i, \quad 1 \le n \le N \tag{16}$$

with $u_0 = \tau_1 = +1$. Having determined all the loop currents, the output power $P_{\text{out},m}$ to the receiver load at cell m is simply given by (6).

To enable calculation of the input power P_{in}, the net input impedance Z_{in} of the generalized MI line seen by the voltage source V_{S} has to be derived. This requires the expression of the effective terminating impedance Z_{eT1} at cell 1, which can be determined using (15) with $n = 1$. Also required is the transfer impedance Z_{Tr1}, which by using (16) can be expressed as

$$Z_{Tr1} = V_{N+1}/I_1 = u_N X\left(\frac{1+\rho_N}{1+\rho_1}\right)e^{-(N-1)\gamma d}\prod_{i=1}^{N} u_{i-1}\tau_i. \tag{17}$$

At the resonance operation, we have $Z_{\text{in}} = Z_{eT1} + R$ for the linear MI lines and $Z_{\text{in}} = Z_{eT1} + Z_{Tr1} + R$ for the circular lines. Since the source current I_{S} supplied by the voltage source V_{S} is given by $I_{\text{S}} = V_{\text{S}}/(Z_{\text{S}} + Z_{\text{in}})$, this yields

$$P_{\text{in}} = |V_{\text{S}}/(Z_{\text{S}} + Z_{\text{in}})|^2 \text{Re}(Z_{\text{in}})\big/2. \tag{18}$$

Following this, the power transfer efficiency to the receiver load at cell m is given by $\eta_m = P_{\text{out},m}/P_{\text{in}}$, and the overall efficiency η of the MI-based DWPT line is equal to the sum of all the transfer efficiencies. Based on the described analysis procedure, two programs were written in Python [34] for theoretical performance calculation of the generalized linear and circular MI waveguide configurations.

B. Efficiency Characteristics of ACMI Lines With Losses

Based on the analysis with the resonator loss model, the efficiency of the proposed ACMI lines can be quantitatively characterized to serve as a guideline for design and implementation in practice. Similar to other DWPT systems, the major mechanism limiting the efficiency stems from losses associated with the coil inductor L, whereas losses due to the capacitor C are much less. With inductor losses dominant, the figure of merit in terms of the normalized quality factor $Q_d = Q/d$ can be utilized to compare various reported resonators in wireless power applications [35], where d is the coil diameter assuming a circular type. For other coil structures, an equivalent dimension $d \approx 2\sqrt{A_{coil}/\pi}$ is employed here, where A_{coil} is the coil area. In essence, Q_d indicates that the total quality factor Q of the resonator is *proportional* to the coil dimension [36], [37]. Thus, in practice, the largest coil dimension allowed by the size of the wirelessly powered moving base should be selected for highest Q and efficiency. For high-frequency operation where losses are mainly due to the skin and proximity effects, Q_d up to 100 cm^{-1}

at 13.56 MHz is feasible, particularly with an air-core inductor [35], [38].

With the use of the analytical formulation with losses in (13)–(18), the efficiency plots (averaged over all cells) versus total number of cells N at different Q values were determined as shown in Fig. 10(a) and (b) for the linear and circular ACMI lines, respectively. In each plot, the range of the quality factor Q starts from the practical value obtained from the corresponding coil implementation in Section V and increases up to three times. Note that a higher quality factor can be achieved by proportionally scaling up the coil dimension (based on the figure of merit Q_d), and/or by making use of an air-core inductor. The plots indicate a lower efficiency at a higher number of cells N, and a higher efficiency at a higher Q. These performance trends are of typical characteristic in DWPT systems. Also, note that more discrepancy between the analytical efficiency plots and simulation/experiment is expected as N becomes larger because the total loss calculation is based on the approximated attenuation constant per cell in (1a). On the contrary, the operation of the ACMI lines to suppress the nulls is unaffected by the approximated phase constant in (1b) since the phase progression per cell is still maintained at $\pi/2$ under the operating resonance frequency ω_0.

For the linear ACMI line with $N = 7$ as in the experiment of Section V, the 10 × 10 cm^2 square planar conductor coil using printed circuit board (PCB) [see Fig. 11(a)] with a simulated $Q = 214$ (or $Q_d = 214/(2\sqrt{100/\pi}) = 18.96\ \text{cm}^{-1}$) was employed. From Fig. 10(a), the calculated efficiency at $\eta \approx 63\%$ can be obtained. Considering the case that the coil dimension is increased to 20 × 20 cm^2 (with fewer turns to maintain the inductance), its quality factor is proportionally increased by twofold, and the efficiency of the linear ACMI line increased to $\eta \approx 79\%$ at $N = 7$ as indicated in Fig. 10(a). By increasing the number of cells to $N = 11$ for more coverage area and track length, the efficiency $\eta \approx 71\%$ is obtained. To maintain the efficiency at $\eta \approx 79\%$ at $N = 11$, the quality factor has to be increased to $Q = 642$. This may be achieved by further enlarging the coil dimension if allowed by the size of the moving base, or by employing an air-core inductor with an inherently higher Q_d than its PCB counterpart [35].

For the circular ACMI line with $N = 7$ in the experiment, the circular-arc PCB coil [see Fig. 11(b)] with a simulated $Q = 211$ ($Q_d = 211/(2\sqrt{95.2/\pi}) = 19.16\ \text{cm}^{-1}$) yields the calculated efficiency at $\eta \approx 63\%$ as indicated by the efficiency plot of Fig. 10(b). To increase the efficiency η up to $\sim$79%, an increase in the quality factor is required by about twofold at $N = 7$ and three-folds at $N = 11$. Similar to the linear ACMI case, this can be achieved by proportionally increasing the coil dimension with more coverage area and track length, and/or making use of an air-core coil implementation.

For the demonstrated DWPT system using the circular ACMI line with $N = 7$ in Section V-D, since the efficiency was calculated at $\eta \approx 63\%$ and the employed moving base consumed up to 1.0 W of power, a 13.56-MHz power amplifier (PA) with more than 1.59 (= 1.0/0.63) W was used. For a real practical scenario, a scaled-up system normally employs a larger coil

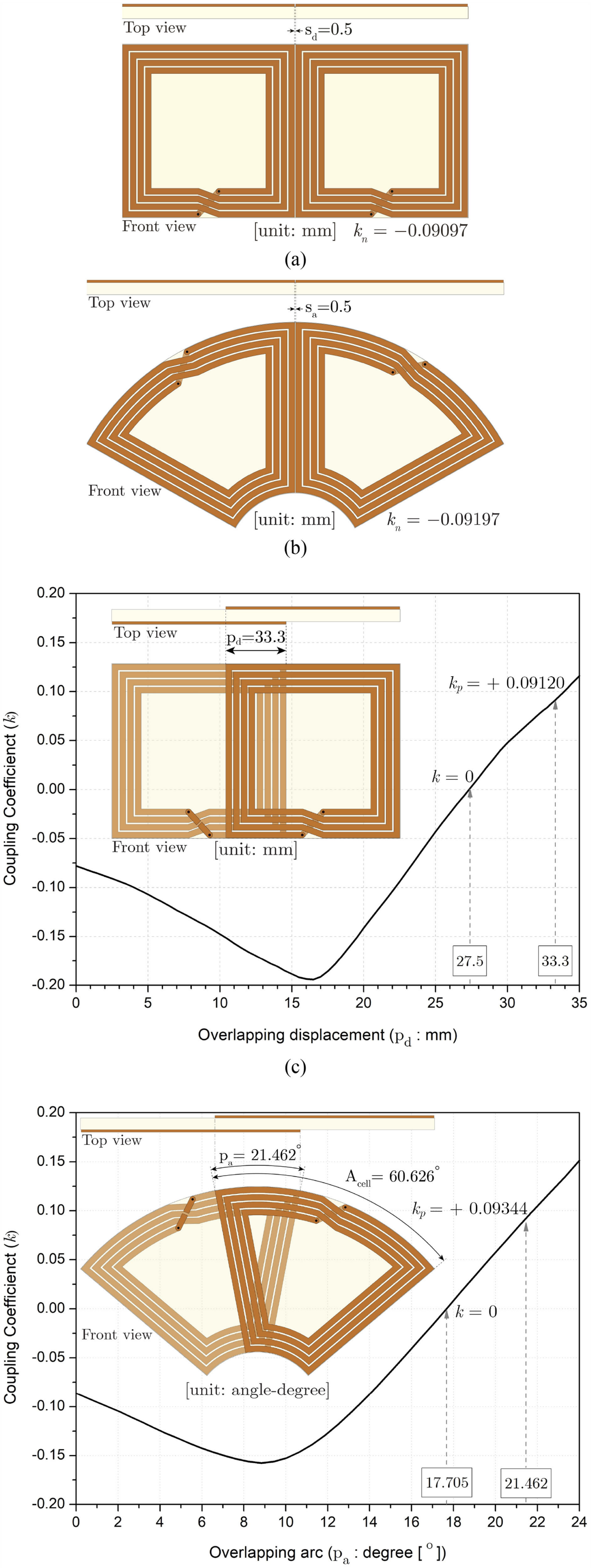

(a)

(b)

(c)

(d)

Fig. 12. Side-by-side coupling geometries for (a) square coils in the linear structure and (b) circular-arc coils in the circular structure. Overlapped coupling geometries and dependence of coupling factors against (c) overlapping displacement [mm] for square coils, and (d) overlapping arc [degree, °] for circular-arc coils.

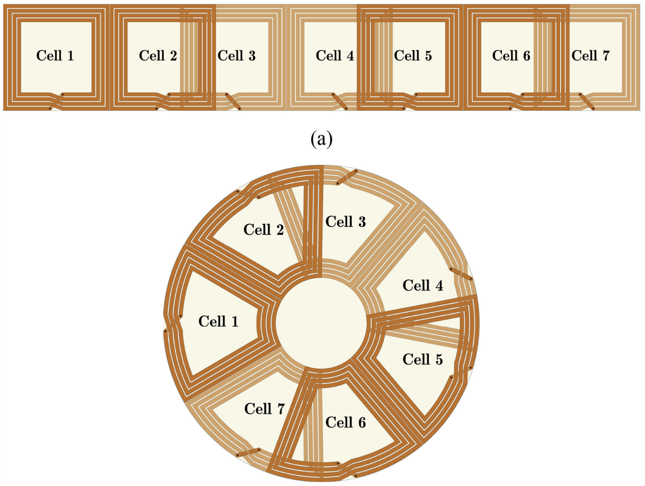

(a)

(b)

Fig. 13. Implementations of the ACMI-based DWPT lines with a total number of cells at $N = 7$ for (a) linear structure ($u_{1,3,5} = -1$ and $u_{2,4,6} = +1$) and (b) circular structure ($u_{1,3,5,7} = -1$ and $u_{2,4,6} = +1$).

dimension, and requires more coverage area, higher efficiency, and higher PA rating. For example, a target practical DWPT system using the circular line may be designed using a larger coil dimension than the prototype coil of Fig. 11(b) by twofold. Based on the figure of merit Q_d, this should yield about two times the quality factor. Given an acceptable efficiency at $\eta = 75\%$, the maximum number of cells is at $N = 9$ as indicated by the efficiency characteristic of Fig. 10(b). With a 20-W consumption in the moving base, a Tx PA with at least 26.6-W power rating is required.

It should be noted that the plots of the average efficiency versus the total cells in Fig. 10 are based on the assumption that the autonomous moving base spends equal time over each resonator cell when traveling along the ACMI lines. From the operational description in Section I, the moving base in fact stops and spends proportionately more time carrying out production tasks at manufacturing stations. Therefore, given the efficiency variation over cell positions of the ACMI lines (as obtained in the experimental results of Section V), the overall efficiency can be further improved by allocating these stations at resonator cells with higher efficiency.

Another viable method to further extend the coverage area while achieving high efficiency is to utilize the linear ACMI configuration in combination with the distributed multi-Tx segmentation [16], [19] to form an effectively longer track in the circular or linear ACMI-based DWPT system. In comparison to the conventional segmentation, significantly fewer multiple Tx power sources are needed, thanks to the null-free power transfer over a number of resonator cells within a single ACMI line segment. This consequently yields a much more relaxed tradeoff between area coverage versus complexity and cost. Note that each multi-Tx segment can be isolated by designing the overlapping distance between the adjacent coils of cells 1 and N of the ACMI lines to obtain zero coupling [see the coupling plots at $k = 0$ in Fig. 12(c) and (d)].

TABLE V
EM SIMULATED ELECTRICAL PARAMETERS OF SELF AND COUPLED COILS AT 13.56-MHZ RESONANCE

Symbol	QUANTITY	Linear Structure	Circular Structure
L	Self Inductance (μH)	2.647	2.440
r_L	Inductor's loss Resistance (Ω)	0.855	0.786
M_n	Side-by-Side Mutual Inductance (μH)	– 0.2408	– 0.2244
k_n	Side-by-Side Coupling Factor	– 0.09097	– 0.09197
M_p	Overlapped Mutual Inductance (μH)	+ 0.2414	+ 0.2280
k_p	Overlapped Coupling Factor	+ 0.09120	+ 0.09344
C_m	Resonant Capacitance (pF)	52.04	56.46
r_C	Capacitor's loss Resistance (Ω)	0.20	0.20

V. IMPLEMENTATION AND VALIDATION

To demonstrate their practical feasibility, the proposed true nulls-free ACMI configurations for DWPT using the linear line structure with quadrature phase termination of Fig. 7(b) and the circular line structure of Fig. 8(b) were implemented and characterized. Comparative performances with their conventional MI counterpart are also provided. The integrity of the extended analysis under lossy conditions is also verified through comparisons between theoretical calculation and measurement. It should be noted that since the implementations were mainly for the demonstration of the nulls-free characteristic, optimization with regard to practical aspects, such as high efficiency and output power, was not taken into account.

A. *Implementation Setup*

For both linear and circular ACMI-based DWPT lines, the total number of cells was selected at $N = 7$, and the resonator coils were fabricated using a 1.6-mm thickness FR4 substrate double-sided PCB with surface mount ceramic chip capacitors soldered in series to tune to the resonant frequency of 13.56 MHz. Note that for a higher first-order coupling factor, lower loss, higher output power, and transfer efficiency, a multilayer PCB with smaller thickness [39]–[41], or air-core coils [35], [38] may be employed for the implementation.

As depicted in Fig. 11(a) for the linear structure, each coil is a 10 × 10 cm^2 four-turn square spiral, with a 3.3-mm trace width and a 1-mm gap. For the circular structure as depicted in Fig. 11(b), each coil is a four-turn 60.626° circular-arc spiral with a 3.5-mm trace width, a 1-mm gap, and inner/outer diameters of 80 mm/280 mm. Table V summarizes the electrical parameters of both coils calculated from electromagnetic (EM) simulation, including the self-inductances, self-capacitances, and effective series loss resistances. Also given are the corresponding series capacitors for a 13.56-MHz resonance.

To form a planar track for DWPT to the planar Rx coils of the moving bases via vertical coupling as illustrated in Fig. 1, the side-way coupled coil arrangement was adopted for the ACMI lines. For the negative coupling factor k_n, the coupled coils were placed side-by-side as shown in Fig. 12(a) and (b) for the square and circular-arc coils, respectively, to obtain the opposite flux linkage direction as described by Fig. 3(b). At a 0.5-mm gap to maximize the coupling magnitude with some margin to account for PCB processing tolerance, the first-order coupling factors was $k_n = -0.09097$ for the coupled square coils, and $k_n = -0.09197$ for the coupled circular-arc coils, as determined from EM simulation.

For the positive coupling factor k_p, the coupled coils were implemented on opposite sides of the 1.6-mm-thick double-sided PCB to enable partial overlapping and the same flux linkage direction similar to the coaxially coupled coils in Fig. 3(c). The coupling factor k_p versus the overlapping displacement ($\mathrm{p_d}$ [mm]) between the square coils and the overlapping arc ($\mathrm{p_a}$ [degree, °]) between the circular-arc coils, as determined from EM simulation, are given in Fig. 12(c) and (d), respectively. Guided by the design condition of identical positive and negative coupling magnitudes, $|k_n| = |k_p|$, $\mathrm{p_d} = 33.3$-mm for $k_p = +0.09120$, and $\mathrm{p_a} = 21.462°$ for $k_p = +0.09344$ were selected for the overlapped coils implementation.

Under the alternate coupling configurations of the square and circular-arc coils of Fig. 12, the second-order coupling factors between nonadjacent coils were simulated at less than 10% and 18%, respectively, of their corresponding first-order couplings. Thanks to the partial overlapping, the second-order couplings were small and can thus be omitted as assumed in the analysis. This assumption was later validated by the measured and simulated results (see Figs. 15–20), which were shown to be in close agreement with the theoretical calculation.

The seven-cell implementation of the linear ACMI-based DWPT line is shown in Fig. 13(a). Due to the use of the overlapping arrangement between the last two coils for a positive coupling factor (u_{N-1} or $u_6 = +1$), the capacitance at the termination cell was set at $C_7 = 47.40$ pF for a negative termination impedance at $-X$, as described in Section III-C. The seven-cell circular ACMI-based DWPT line is shown in Fig. 13(b). The Rx cells for both implementations were of their corresponding 13.56-MHz resonance coil types, with an added series load resistance equal to their associated characteristic impedance R_0. Following this, the magnitude of the Rx coupling factor $|k_X|$ that approximately yields the referred impedance R_0 at the loaded cell is the same as that of the mutual coupling $|k|$ (with $|k_n| \approx |k_p|$) between adjacent cells for each implementation. Table VI summarizes all the equivalent circuit parameters, including the effective series loss resistance r_C (at ~0.20 Ω) in the selected chip capacitors. These parameters were employed for theoretical performance calculation of the implemented linear and circular lines using the analysis described in Section IV-A.

TABLE VI
SUMMARY OF EQUIVALENT CIRCUIT PARAMETERS FOR THEORETICAL CALCULATION OF LINEAR AND CIRCULAR ACMI-BASED DWPT LINES

Parameters	Linear Structure	Circular Structure
ω_0 (rad/s)	$2\pi \times 13.56 \times 10^6$	$2\pi \times 13.56 \times 10^6$
L (H)	2.647×10^{-6}	2.440×10^{-6}
C_m (F)	52.04×10^{-12}	56.46×10^{-12}
$R = r_L + r_C$ (Ω)	1.055	0.986
$\lvert k\rvert = (\lvert k_n\rvert + \lvert k_p\rvert)/2$	0.09108	0.09267
R_0 (Ω)	20.54	19.11
X (Ω)	$+20.54j$	$+19.11j$

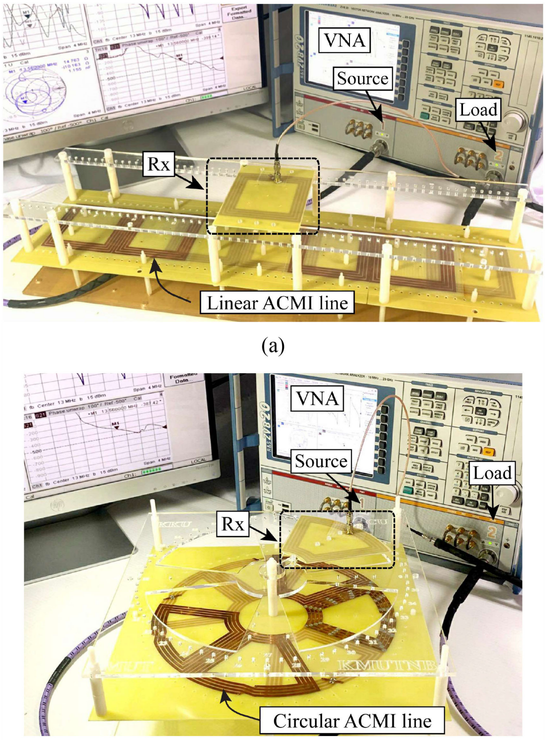

(a)

(b)

Fig. 14. Experimental setup for S-parameters measurement of (a) linear and (b) circular ACMI-based DWPT lines.

B. Measurement Setup

The experiments were set up as shown in Fig. 14(a) and (b) for the linear and circular ACMI-based DWPT lines, respectively. A Rohde and Schwartz model ZVB20 vector network analyzer was employed with Port 1 serving as the Tx source and Port 2 as the Rx load. Through the measured two-port scattering or S-parameters with a 50-Ω reference impedance (Z_ref), the devices' performances in terms of the power transfer efficiency and load power normalized to the available source power were characterized.

As noticed in Fig. 14, a transparent acrylic sheet (with laser milled holes and openings) was placed above each of the structures by nonmetal standoffs to support both horizontal (x-axis for the linear structure, and ρ-axis in the cylindrical coordinate for the circular structure) and vertical (z-axis) movements of the receiver. At a specified height, which determines the mutual coupling between the DWPT line and its receiver, the corresponding S-parameters were measured and recorded at each of the specified Rx positions along their full straight/arc lengths. Subsequently, the power transfer efficiency (η) was calculated by [42]

$$\eta = \frac{P_{\text{out}}}{P_{\text{in}}} = \frac{|S_{21}|^2}{|1 - S_{22}\Gamma_{\text{L}}|^2} \cdot \frac{1 - |\Gamma_{\text{L}}|^2}{1 - |\Gamma_{\text{in}}|^2} \tag{19}$$

and the normalized output power $P_{\text{out}}/P_{\text{avl}}$ by

$$\frac{P_{\text{out}}}{P_{\text{avl}}} = \eta(1 - |\Gamma_{\text{in}}|^2) \cdot \frac{|1 - \Gamma_{\text{S}}|^2}{|1 - \Gamma_{\text{in}}\Gamma_{\text{S}}|^2} \tag{20}$$

where $\Gamma_{\text{S}} = (Z_{\text{S}} - Z_{\text{ref}})/(Z_{\text{S}} + Z_{\text{ref}}), \Gamma_{\text{L}} = (Z_{\text{L}} - Z_{\text{ref}})/(Z_{\text{L}} + Z_{\text{ref}})$, and $\Gamma_{\text{in}} = S_{11} + [S_{12}S_{21}\Gamma_{\text{L}}/(1 - S_{22}\Gamma_{\text{L}})]$, with the specified source impedance Z_{S} and receiver's load impedance Z_{L} of the linear and circular structures typically different from $Z_{\text{ref}} = 50\ \Omega$. Note that the device performances can also be calculated by postprocessing the measured S-parameters in the Keysight Advanced Design System tool [43].

C. Performance Results and Comparison

1) Linear ACMI-Based DWPT Line: For the linear nulls-free ACMI line, the Rx locations for measurement were specified by dividing its length between the centers of the Tx cell 1 and the termination cell 7 (see Fig. 13) into 50 uniform steps yielding the normalized Rx positions 0–50, as shown along the x-axis of Fig. 15. The nominal Rx height that yielded $|k_X| \approx |k|$ was determined at 65.0 mm based on EM simulation of two axially aligned coupled square coils. The load impedance Z_{L} at the Rx was set to be purely resistive at $Z_{\text{L}} = R_{\text{L}} = R_0 = 20.54\ \Omega$ as indicated in Table VI, and the source impedance Z_{S} was equal to the real part of the average input impedance over all the Rx positions.

At the nominal height of 65.0 mm, the measured efficiency (η) and normalized load power ($P_{\text{out}}/P_{\text{avl}}$) at 13.56 MHz versus the normalized Rx positions are given in Fig. 15(a) and (b), respectively. Also included for comparison are the results based on EM simulation using Computer Simulation Technology software [44] and the extended analytical equations in Section IV-A, applicable particularly at the centers of each cell.

As evident from Fig. 15(a) and (b), the measured results of the linear ACMI line (thick black solid lines) exhibit nulls-free characteristics over the entire Rx positions, with the power transfer efficiency from 55% up to 71%, and the delivered load power from 50% up to 69% of the available source power. The obtained levels of performance are mainly determined by losses associated with the square coils. The average measured efficiency was calculated at 64% and the average normalized load power at 60% over all the Rx positions. Note the measured results are in excellent agreement with those obtained from EM simulation (red lines), and in close agreement with the theoretical calculation (circles). Also, note that the symbol positions correspond to the centers of the cells.

Also shown in the figures are the measured and simulated results (black solid/dash lines), as well as theoretical results (squares) of the seven-cell conventional MI-based DWPT line implemented using the same square coils with only the side-by-side couplings. The performance nulls at periodic receiver positions are clearly noticed. It should be noted that the peak power efficiency and normalized power in the conventional line are higher because those nulled cells with near-zero circulating loop currents contribute practically no power loss. Also note that the discrepancies between the measured/simulated and theoretical results are somewhat higher in the linear nulls-free ACMI line, as compared to its MI counterpart. This is mainly attributed to the overlapped coupling arrangement and relatively higher second-order mutual couplings associated with the alternate coupling coils of the ACMI waveguide structure, which were not taken into account in the analysis.

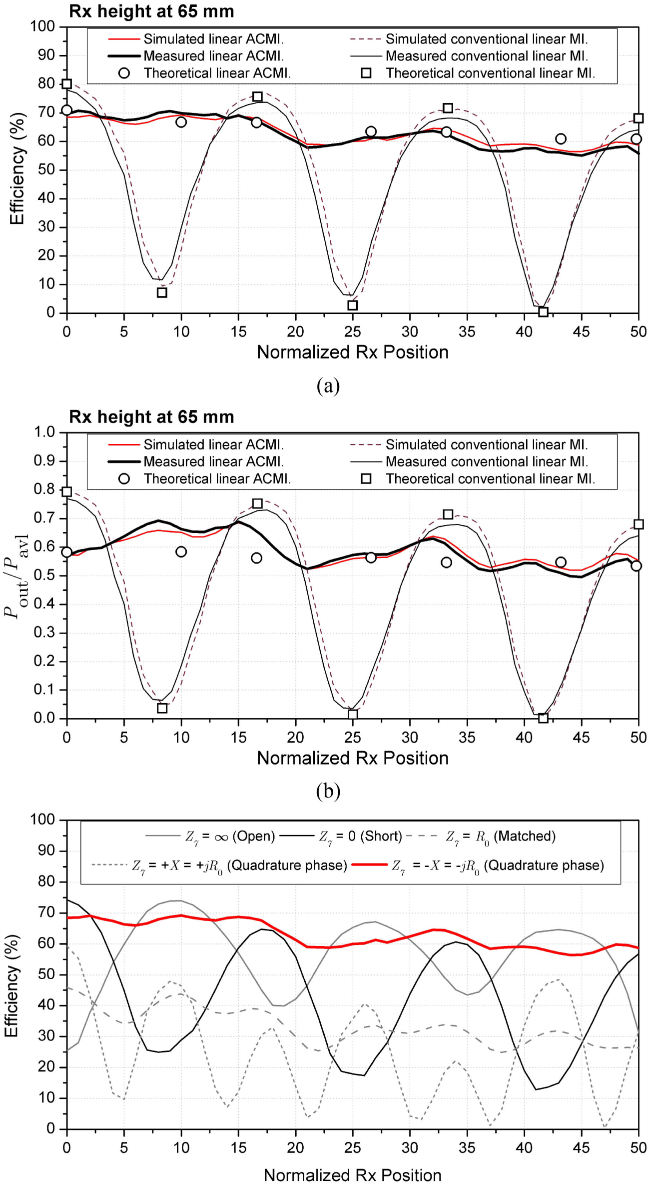

(a)

(b)

(c)

Fig. 15. Measured, simulated results (lines), and theoretical results (points) at Rx height of 65.0 mm of linear ACMI-based DWPT structure with quadrature phase termination: (a) power transfer efficiency and (b) normalized output load power. Also included are the results from measurement/simulation (lines) and theory (points) of conventional linear MI counterpart. Circle and square positions correspond to the cell centers. (c) Simulated transfer efficiency of the linear ACMI line with last cell at $Z_7 = 0$ (short), R_0 (matched) $\pm jR_0$ (quadrature phase), and ∞ (open) terminations.

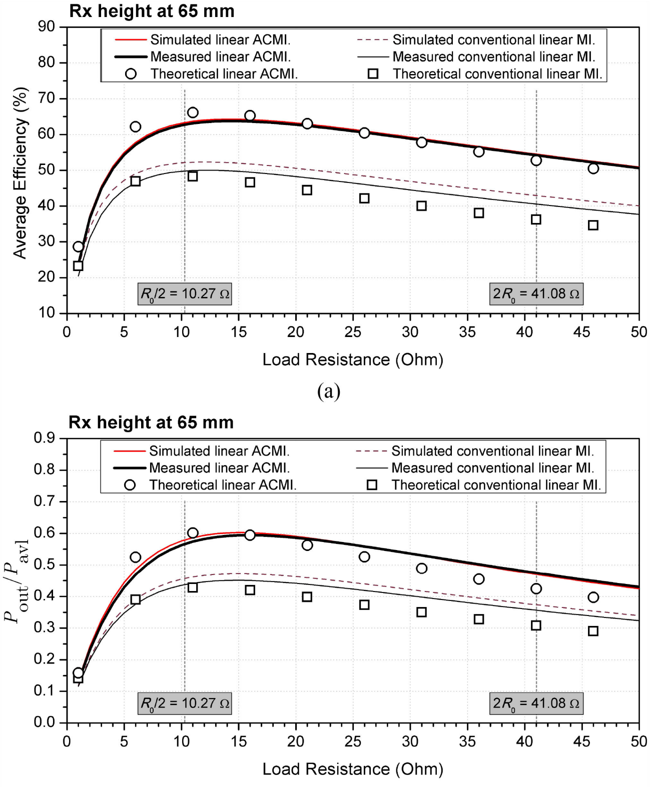

Fig. 16. Load regulation performance of the linear MI- and ACMI-based DWPT lines in terms of (a) average efficiency versus load resistance R_{L} and (b) average normalized power versus load resistance R_{L}, from theoretical analysis (points), measurement, and simulation (lines).

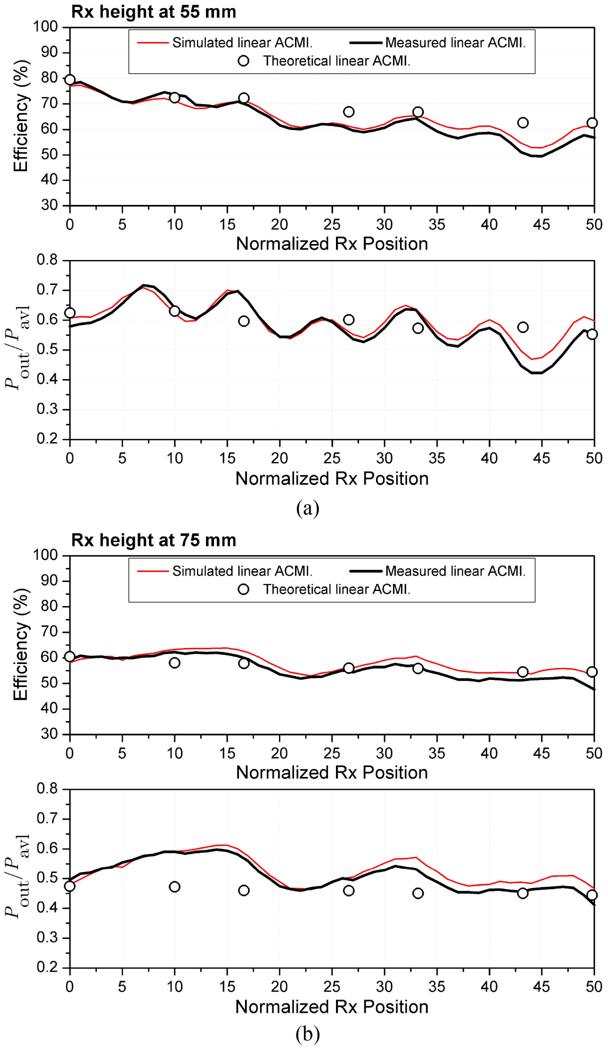

Fig. 17. Results from measurement and simulation (lines), as well as theory (circles) for power transfer efficiency and normalized load power of linear ACMI structure with quadrature phase termination at (a) 55-mm Rx height and (b) 75-mm Rx height. Circle positions correspond to the cell centers.

It is also instructive to show in Fig. 15(c) that the simulated efficiency results of the linear ACMI line with open/short/ matched terminations, together with the two quadrature termination conditions (at $Z_N = \pm X = \pm jR_0$). As theorized in the analysis, only the quadrature termination at $Z_N = -X = -jR_0$ in the last cell 7 yields a true nulls-free characteristic because this provides the alternate phase polarity in the reflected MIW with reference to the incoming MIW from the previous cell 6 [see Fig. 6(b) for $u_{N-1} = +1$].

To analyze the load regulation performance of the linear MI- and ACMI-based DWPT lines, the dependence of the efficiency and normalized power against the load resistance R_L of the Rx coil were characterized. To take the free-positioning of the load into account, the analysis was based on the average performance over the Rx coil locations for each load resistance.

Fig. 16(a) shows the average efficiency (η_{avg}) versus R_{L} for the linear ACMI line via the theoretical calculation (circles), averaged over the Rx locations at the cell centers. Also given with close agreement are the measured and simulated load regulation performances (black/red solid lines) based on the average efficiency over *all* the Rx coil locations along the line. A small variation in the measured average efficiency between 55% and 64% can be observed over R_{L} ranging from $R_0/2$ to $2R_0$ for half and twice load conditions, respectively. The load regulation of the conventional linear MI line was also characterized via the theoretical analysis (squares), measurement, and simulation (black solid/dash lines), as also included in Fig. 16(a). Although a similar variation was observed, the average efficiency of the conventional line is smaller due to its inherent periodic power nulls. Fig. 16(b) shows the load regulation in terms of the average normalized power ($P_{\mathrm{out}}/P_{\mathrm{avl}}$) against R_L. Performance trends similar to Fig. 16(a) can be observed, with a variation in the measured average normalized power between 48% and 60% for the linear ACMI line over the R_L range.

Fig. 17(a) and (b) shows the measured results of the linear ACMI line (black solid lines) at the Rx heights of 65.0 ± 10.0 mm, i.e., at 55.0 mm and 75.0 mm, respectively. At both heights, the null-free performance characteristics are maintained over the normalized Rx locations, with the power efficiency from 48% up to 79%, and the normalized load power from 42% up to 72%. Again, the measured results are in excellent agreement with EM simulation (red lines), in close agreement with the theoretical calculation (circles). It is also observed from Figs. 15 and 17 that the efficiency and power performances tend to decrease at

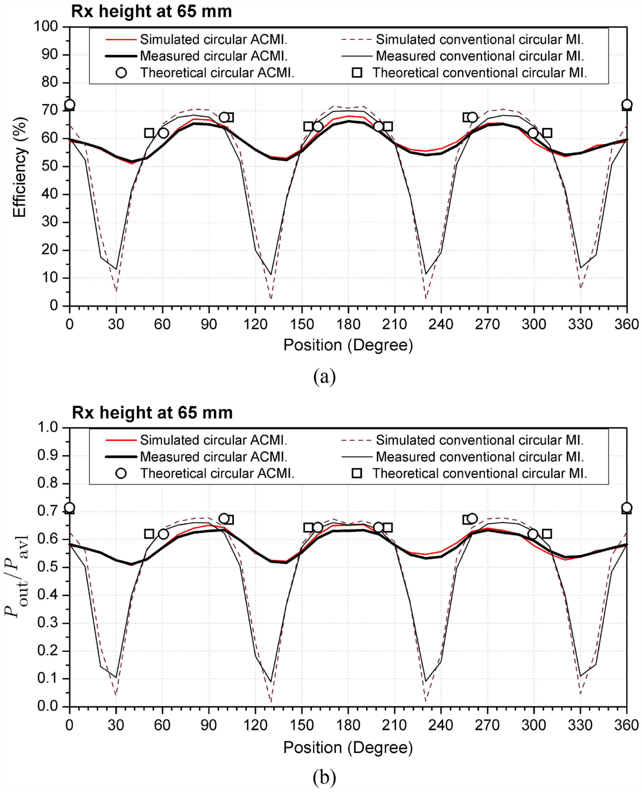

(a)

(b)

Fig. 18. Measured, simulated results (lines), and theoretical results (points) of (a) efficiency and (b) normalized load power for the circular ACMI-based DWPT line at receiver height of 65.0 mm. Also included are the results from measurement, simulation (lines), and theory (points) of MI-based circular counterpart. Circle and square positions correspond to the cell centers.

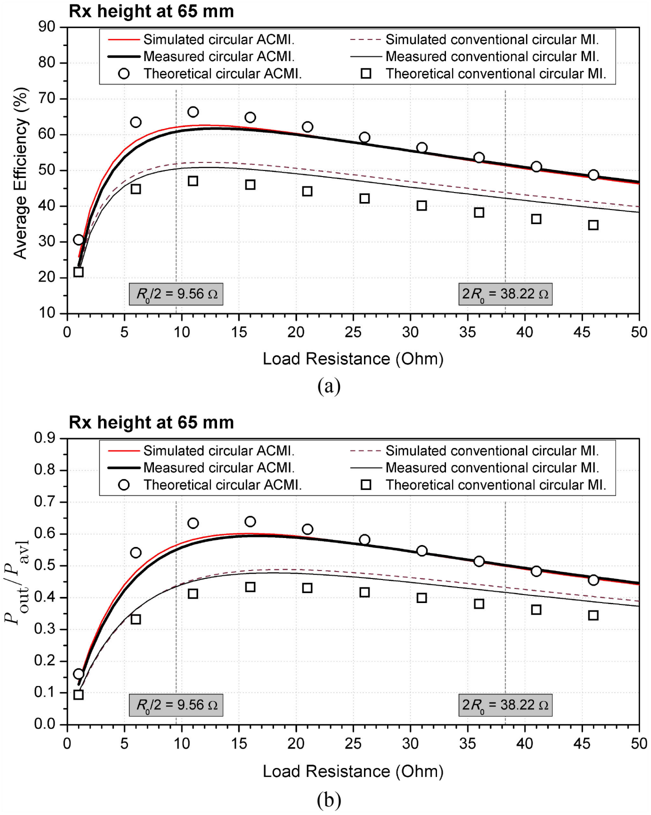

(a)

(b)

Fig. 19. Load regulation performance of the circular MI- and ACMI-based DWPT lines in terms of (a) average efficiency versus load resistance R_{L} and (b) average normalized power versus load resistance R_{L}, from theoretical analysis (points), measurement, and simulation (lines). For the circular MI line, the performances at half-cell location were assumed zero and included in the theoretical analysis to account for its power nulls characteristic.

a Rx position away from the Tx cell. This is due to losses as the MIWs propagated down the line to the termination cell.

2) Circular ACMI-Based DWPT Line: The normalized Rx positions for measurement of the nulls-free circular DWPT line were specified by dividing its full arc-length along the ρ-axis into 36 uniform positions at angles between 0° and 360° from the center of the transmitter cell 1 back to the same position. Similar to its linear counterpart, the nominal height that yielded $|k_X| \approx |k|$ was determined at 65.0 mm. The load impedance was set at $R_L = R_0 = 19.11\ \Omega$ as given in Table VI, whereas the source impedance Z_{S} was determined by the complex conjugate of the average input impedance over all the Rx positions.

At the nominal height and 13.56 MHz operation, the efficiency (η) and normalized load power ($P_{\text{out}}/P_{\text{avl}}$) versus the Rx positions of the circular ACMI-based DWPT lines are shown in Fig. 18(a) and (b), respectively. The measured results are indicated by thick black solid lines, simulated results by red lines, and analytically calculated results by circles. The angle positions corresponding to the cell centers are also indicated by the circles in the figures. The measurement showed the power transfer efficiency from 52% up to 66%, and the load power from 51% to 63% of the available source power. The average measured efficiency was calculated at 59% and the average normalized load power at 58% over all the Rx positions. Also included in Fig. 18 are the measured and simulated results (black solid/dash lines), as well as theoretical results (squares) of the seven-cell circular MI counterpart with only the side-by-side couplings. Clearly, the periodic performance nulls are observed at the Rx positions between the cells that possesses out-of-phase total loop currents.

The same load regulation analysis similar to the linear implementation was applied to the circular MI and ACMI lines, as shown by in the average efficiency (η_{avg}) and normalized power ($P_{\text{out}}/P_{\text{avl}}$) versus the load resistance R_L in Fig. 19(a) and (b), respectively. Based on the measurement, the circular ACMI line exhibits an efficiency variation between 51% and 62%, and a normalized power variation between 50% and 59%, over R_L ranging from $R_0/2$ to $2R_0$. For the circular MI counterpart, although indicating similar variations, the measured average efficiency and normalized power are smaller due to its power nulls characteristic.

For the Rx height at 55.0 and 75.0 mm, the measured results of the circular ACMI line are shown in Fig. 20(a) and (b), indicating the nulls-free characteristic with the efficiency between 48% and 70%, and the normalized load power between 47% and 66%. Also, the measured average efficiency was more than 55% and the average normalized load power more than 55%. As evident from Figs. 18–20, all the measured results are in excellent agreement with EM simulation, and in close agreement with the analytical calculation. It should be noted that, unlike its

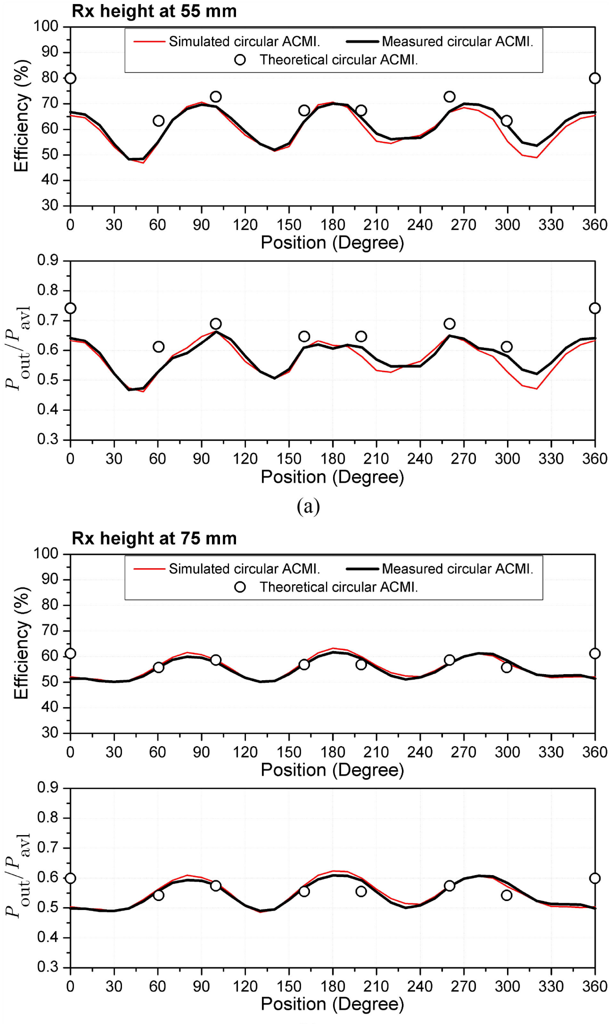

(a)

(b)

Fig. 20. Results from measurement and simulation (lines), as well as theory (circles) of efficiency and normalized load power at Rx height of (a) 55.0 mm and (b) 75.0 mm for the circular ACMI line. Circle positions correspond to the cell centers.

linear counterpart, no performance attenuation trend against the Rx position was observed in the circular line. This should be attributed to its two-path power transfer operation via both the CW and CCW directions, where each path experienced periodic power nulls and hence less power loss before reaching the load.

D. Demonstration Model of Batteryless DWPT System

Fig. 21 shows a scaled-down model of the batteryless DWPT system of Fig. 1 utilizing the seven-cell circular ACMI waveguide of Fig. 14(b) at a 13.56-MHz operating frequency. As compared to a kHz operation, a MHz operation is more suitable for the DWPT system because the Rx coil of the moving base can be implemented with a few turns, yielding a more compact and lighter weight Rx coil. For ease of implementation, the moving base was made of one wheel driven by a dc motor, with a diode rectifier, a dc–dc converter, and an Arduino board for motor speed and direction controls. Its power consumption during the operation was up to 1.0 W. The base was attached to the Rx coil along a rotating shaft and entirely powered by the circular ACMI waveguide located at a 65-mm gap underneath. An off-the-shelf PA was used as the single Tx source.

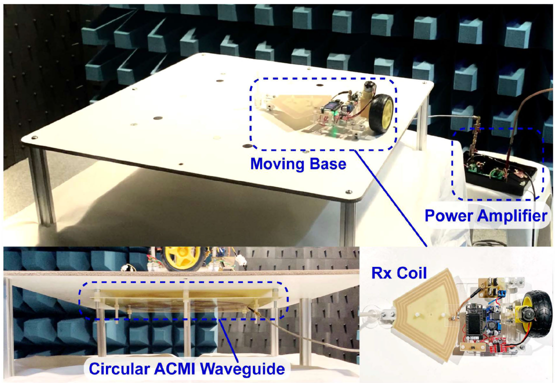

Fig. 21. Experimental batteryless DWPT system model for demonstration of nulls-free continuous power transfer using the implemented circular ACMI waveguide.

To validate the feasibility of delivering continuous power along the track with no use of batteries, demo experiments of the DWPT system with one and two moving bases were conducted, and can be watched in Supplementary Video. It should be noted that, being a fully passive component with no use of active circuitry, the true nulls-free ACMI lines can be readily scaled up for real industrial applications with higher power delivery demand beyond the demonstration model.

VI. CONCLUSION

The ACMI waveguides have been developed and theoretically analyzed. Their true nulls-free characteristics with no requirement of active circuitry have been experimentally demonstrated through implementations of the linear and circular ACMI lines, as well as the experimental model of a batteryless DWPT system. As compared to previous methods for DWPT applications, the ACMI lines strike a balance between low complexity and low cost of the single Tx coil configuration, and low leakage and low emission of the segmented multiple active Tx coil configuration. This allows for more flexible tradeoffs between complexity, cost, and efficiency in a practical DWPT system design.

The set of closed-form analytical equations derived in this work has provided insight into the operation of the ACMI lines for DWPT. It can also be employed to facilitate design optimization without resort to time-consuming simulation, and enable investigation on their performance tradeoffs. In this regard, numerical calculation using the analysis programs coded in Python revealed that the nulls-free characteristic of the ACMI lines is maintained under multiple receivers, albeit with more variation in the efficiency. This performance characteristic has been confirmed via simulation. In addition, the derived equations have the potential to analyze ACMI waveguides beyond one dimension, as already demonstrated in the case of the circular line structure.

Due to its near phase-coherent magnetic field distribution, the ACMI lines hold promise for various emerging DWPT applications, particularly those that make use of one single Tx to emit MIWs to wirelessly deliver both power and data over a wide coverage area to free-positioned Rx. Since the idea of limiting phase progression of propagating waves employed in the ACMI waveguides is general, it is also envisioned to have applications on other types of wave media to mitigate power nulling due to standing waves.

ACKNOWLEDGMENT

The authors would like to thank the anonymous reviewers for their invaluable suggestions. They would also like to thank T. Chotsiri of Group Maker for his support on the hardware implementation of the batteryless DWPT demonstration.

REFERENCES

[1] A. Kurs, A. Karalis, R. Moffatt, J. D. Joannopoulos, P. Fisher, and M. Soljavci, "Wireless power transfer via strongly coupled magnetic resonances," *Science*, vol. 317, no. 5834, pp. 83–86, Jul. 2007.

[2] N. Tesla, "The transmission of electric energy without wires," *Elect. World Eng.*, vol. 5, pp. 162–167, 1904.

[3] X. Liu and S. Y. Hui, "Optimal design of a hybrid winding structure for planar contactless battery charging platform," *IEEE Trans. Power Electron.*, vol. 23, no. 1, pp. 455–463, Jan. 2008.

[4] B. L. Cannon, J. F. Hoburg, D. D. Stancil, and S. C. Goldstein, "Magnetic resonant coupling as a potential means for wireless power transfer to multiple small receivers," *IEEE Trans. Power Electron.*, vol. 24, no. 7, pp. 1819–1825, Jul. 2009.

[5] S. Y. Hui, "Planar wireless charging technology for portable electronic products and Qi," *Proc. IEEE*, vol. 101, no. 6, pp. 1290–1301, Jun. 2013.

[6] S. Y. R. Hui, W. Zhong, and C. K. Lee, "A critical review of recent progress in mid-range wireless power transfer," *IEEE Trans. Power Electron.*, vol. 29, no. 9, pp. 4500–4511, Sep. 2014.

[7] W. X. Zhong, X. Liu, and S. Y. R. Hui, "A novel single-layer winding array and receiver coil structure for contactless battery charging systems with free-positioning and localized charging features," *IEEE Trans. Ind. Electron.*, vol. 58, no. 9, pp. 4136–4144, Sep. 2011.

[8] U. K. Madawala and D. J. Thrimawithana, "A bidirectional inductive power interface for electric vehicles in V2G systems," *IEEE Trans. Ind. Electron.*, vol. 58, no. 10, pp. 4789–4796, Oct. 2011.

[9] A. K. RamRakhyani, S. Mirabbasi, and M. Chiao, "Design and optimization of resonance-based efficient wireless power delivery systems for biomedical implants," *IEEE Trans. Biomed. Circuits Syst.*, vol. 5, no. 1, pp. 48–63, Feb. 2011.

[10] C. C. Mi, G. Buja, S. Y. Choi, and C. T. Rim, "Modern advances in wireless power transfer systems for roadway powered electric vehicles," *IEEE Trans. Ind. Electron.*, vol. 63, no. 10, pp. 6533–6545, Oct. 2016.

[11] Y. Li *et al.*, "A new coil structure and its optimization design with constant output voltage and constant output current for electric vehicle dynamic wireless charging," *IEEE Trans. Ind. Informat.*, vol. 15, no. 9, pp. 5244–5256, Sep. 2019.

[12] S. A. Mirbozorgi, H. Bahrami, M. Sawan, and B. Gosselin, "A smart cage with uniform wireless power distribution in 3D for enabling long-term experiments with freely moving animals," *IEEE Trans. Biomed. Circuits Syst.*, vol. 10, no. 2, pp. 424–434, Apr. 2016.

[13] Q. Xu, Z. Gao, H. Wang, J. He, Z. H. Mao, and M. Sun, "Batteries not included: A mat-based wireless power transfer system for implantable medical devices as a moving target," *IEEE Microw. Mag.*, vol. 14, no. 2, pp. 63–72, Mar. 2013.

[14] H. H. Wu, G. A. Covic, J. T. Boys, and D. J. Robertson, "A series-tuned inductive-power-transfer pickup with a controllable ac-voltage output," *IEEE Trans. Power Electron.*, vol. 26, no. 1, pp. 98–109, Jan. 2011.

[15] J. P. C. Smeets, T. T. Overboom, J. J. Jansen, and E. A. Lomonova, "Comparison of position-independent contactless energy transfer systems," *IEEE Trans. Power Electron.*, vol. 28, no. 4, pp. 391–399, Apr. 2013.

[16] A. Pacini, A. Costanzo, S. Aldhaher, and P. D. Mitcheson, "Load- and position-independent moving MHz WPT system based on GaN-distributed current sources," *IEEE Trans. Microw. Theory Techn.*, vol. 65, no. 12, pp. 5367–5376, Dec. 2017.

[17] S. A. Mirbozorgi, H. Bahrami, M. Sawan, and B. Gosselin, "A smart multicoil inductively coupled array for wireless power transmission," *IEEE Trans. Ind. Electron.*, vol. 61, no. 11, pp. 6061–6070, Nov. 2014.

[18] P. K. S. Jayathurathnage, A. Alphones, D. M. Vilathgamuwa, and A. Ong, "Optimum transmitter current distribution for dynamic wireless power transfer with segmented array," *IEEE Trans. Microw. Theory Techn.*, vol. 66, no. 1, pp. 346–356, Jan. 2018.

[19] S. Huh and D. Ahn, "Two-transmitter wireless power transfer with optimal activation and current selection of transmitters," *IEEE Trans. Power Electron.*, vol. 33, no. 6, pp. 4957–4967, Jun. 2018.

[20] J. W. Kim *et al.*, "Wireless power transfer for free positioning using compact planar multiple self-resonators," in *Proc. IEEE MTT-S Int. Microw. Workshop Ser. Innov. Wireless Power Transmiss., Technol., Syst., Appl.*, May 2012, pp. 127–130.

[21] B. Wang, W. Yerazunis, and K. H. Teo, "Wireless power transfer: Metamaterials and array of coupled resonators," *Proc. IEEE*, vol. 101, no. 6, pp. 1359–1368, Jun. 2013.

[22] C. J. Stevens, "Power transfer via metamaterials," *Comput., Mater. Continua*, vol. 33, no. 1, pp. 1–18, 2013.

[23] C. J. Stevens, "Magnetoinductive waves and wireless power transfer," *IEEE Trans. Power Electron.*, vol. 30, no. 11, pp. 6182–6190, Nov. 2015.

[24] G. Puccetti, C. J. Stevens, U. Reggiani, and L. Sandrolini, "Experimental and numerical investigation of termination impedance effects in wireless power transfer via metamaterial," *Energies*, vol. 8, no. 3, pp. 1882–1895, 2015.

[25] F. S. Sandoval, S. M. T. Delgado, A. Moazenzadeh, and U. Wallrabe, "Nulls-free wireless power transfer with straightforward control of magnetoinductive waves," *IEEE Trans. Microw. Theory Techn.*, vol. 65, no. 4, pp. 1087–1093, Apr. 2017.

[26] F. S. Sandoval, S. M. T. Delgado, A. Moazenzadeh, and U. Wallrabe, "A 2-D magnetoinductive wave device for freer wireless power transfer," *IEEE Trans. Power Electron.*, vol. 34, no. 11, pp. 10433–10444, Nov. 2019.

[27] C. K. Lee, W. X. Zhong, and S. Y. R. Hui, "Effects of magnetic coupling of nonadjacent resonators on wireless power domino-resonator systems," *IEEE Trans. Power Electron.*, vol. 27, no. 4, pp. 1905–1916, Apr. 2012.

[28] X. Zhang, S. L. Ho, and W. N. Fu, "Quantitative design and analysis of relay resonators in wireless power transfer system," *IEEE Trans. Magn.*, vol. 48, no. 11, pp. 4026–4029, Nov. 2012.

[29] W. Zhong, C. Lee, and R. Hui, "General analysis on the use of tesla's resonators in domino forms for wireless power transfer," *IEEE Trans. Ind. Electron.*, vol. 60, no. 1, pp. 261–270, Jan. 2013.

[30] F. Jolani, Y.-Q. Yu, and Z. Chen, "A planar magnetically-coupled resonant wireless power transfer using array of resonators for efficiency enhancement," in *Proc. IEEE MTT-S Int. Microw. Symp.*, May 2015, pp. 1–4.

[31] E. Shamonina, V. A. Kalinin, K. H. Ringhofer, and L. Solymar, "Magnetoinductive waves in one, two, and three dimensions," *J. Appl. Phys.*, vol. 92, no. 10, pp. 6252–6261, Nov. 2002.

[32] R. R. A. Syms, E. Shamonina, and L. Solymar, "Magneto-inductive waveguide devices," *IEE Proc.-Microw. Antennas Propag.*, vol. 153, no. 2, pp. 111–121, Apr. 2006.

[33] L. Solymar, *Waves in Metamaterials*. London, U.K.: Oxford Univ. Press, 2009.

[34] Python, Python Programming Language, Python Software Foundation, 2021. [Online]. Available: http://www.python.org

[35] G. Zulauf and J. M. Rivas-Davila, "Single-turn air-core coils for high-frequency inductive wireless power transfer," *IEEE Trans. Power Electron.*, vol. 35, no. 3, pp. 2917–2932, Mar. 2020.

[36] D. Perreault *et al.*, "Opportunities and challenges in very high frequency power conversion," in *Proc. 24th Annu. IEEE Appl. Power Electron. Conf. Expo.*, Feb. 2009, pp. 1–14.

[37] A. L. Stein, P. A. Kyaw, and C. R. Sullivan, "Wireless power transfer utilizing a high-Q self-resonant structure," *IEEE Trans. Power Electron.*, vol. 34, no. 7, pp. 6722–6735, Jul. 2019.

[38] J. M. Arteaga, S. Aldhaher, G. Kkelis, D. C. Yates, and P. D. Mitcheson, "Multi-MHz IPT systems for variable coupling," *IEEE Trans. Power Electron.*, vol. 33, no. 9, pp. 7744–7758, Sep. 2018.

[39] U. M. Jow and M. Ghovanloo, "Design and optimization of printed spiral coils for efficient transcutaneous inductive power transmission," *IEEE Trans. Biomed. Circuits Syst.*, vol. 1, no. 3, pp. 193–202, Sep. 2007.

[40] F. S. Sandoval, A. Moazenzadeh, and U. Wallrabe, "Comprehensive modelling of magnetoinductive wave devices for wireless power transfer," *IEEE Trans. Power Electron.*, vol. 33, no. 10, pp. 8905–8915, Oct. 2018.

[41] S. Raju, R. Wu, M. Chan, and C. P. Yue, "Modeling of mutual coupling between planar inductors in wireless power applications," *IEEE Trans. Power Electron.*, vol. 29, no. 1, pp. 481–490, Jan. 2014.

[42] D. M. Pozar, *Microwave Engineering*. New York, NY, USA: Wiley, 1998.

[43] Keysight Technologies, *ADS (Advanced Design System)*. Santa Rosam, CA, USA: Keysight Technol., 2009.

[44] CST Microwave Studio, Computer Simulation Technology, Framing-Ham, MA, USA, 2019.

Chawalit Rakluea (Student Member, IEEE) received the B.Eng. (Hons.) and M.Eng. degrees in electrical engineering (telecommunication), in 2009 and 2012, respectively, from the King Mongkut's University of Technology North Bangkok, Bangkok, Thailand, where he is currently working toward the Ph.D. degree in electrical engineering.

Since 2012, he has been a Lecturer with the Rajamangala University of Technology Thanyaburi (RMUTT), Thailand. His research interests include wireless power transmission, metamaterials, metasurface, and antenna technology.

Apisak Worapishet (Senior Member, IEEE) received the B.Eng. (Hons.) degree from the King Mongkut's Institute of Technology Ladkrabang, Bangkok, Thailand, in 1990, the M.Eng.Sc. degree from the University of New South Wales, Kensington, NSW, Australia, in 1995, and the Ph.D. degree from the Imperial College London, London, U.K., in 2000, all in electrical engineering.

Since 1990, he has been with the Mahanakorn University of Technology, Bangkok, Thailand, where he is currently a Professor of electronic engineering. He is also the Director of the Mahanakorn Microelectronics Research Center and a Lecturer with the Mahanakorn Institute of Innovation, Bangkok, Thailand. His research interests include analog integrated circuits, passive/active RF/microwave circuits, and wireless power transfer.

Dr. Worapishet has been an Associate Editor for the IEEE TRANSACTIONS ON CIRCUITS AND SYSTEMS I: REGULAR PAPERS since 2016. He was the Editor-in-Chief for *ECTI Transactions on Electrical Engineering, Electronics, and Communications* from 2012 to 2019. He is a member of the Analog Signal Processing Technical Committee and the IEEE Circuits and Systems Society. He was the recipient of the British Council Researcher Exchange Program Award in 2009.

Sarawuth Chaimool (Senior Member, IEEE) received the B.Eng., M.Eng., and Ph.D. degrees in electrical engineering from the King Mongkut's University of Technology North Bangkok (KMUTNB), Bangkok, Thailand.

From 2004 to 2014, he was a Lecturer with the Department of Electrical Engineering, KMUTNB. From 2014 to 2016, he was with Udon Thani Rajabhat University. He is currently an Associate Professor with Khon Kaen University, Khon Kaen, Thailand. He has authored or coauthored about 120 publications, 3 chapter books, and 2 academic books, including *Antenna Engineering (in Thai) (KMUTNB, 2013) and Electromagnetic Engineering (in Thai) (KMUTNB 2014)*. His current research interests include metamaterials and metasurfaces, 5G/6G metasurface reflectors, wireless power transfer, advanced antenna designs, and passive microwave circuits. Moreover, he teaches and contributes to Youtube (Jaounarak), Facebook (EMETARA), and website (metaradiator).

Dr. Chaimool is a member of ECTI Thailand and EEAAT Thailand. He is also a Founding Member of the Innovative Electromagnetic Academic of Thailand (iEMAT) and an Editor for Cogent Engineering. He is an active reviewer for numerous IEEE, IET, Elsevier, IOP science, and other international journals.

Yan Zhao (Senior Member, IEEE) received the B.Sc. degree from the Beijing University of Posts and Telecommunications, Beijing, China, the M.Sc. degree from the University of Birmingham, Birmingham, U.K., and the Ph.D. degree from Queen Mary, University of London, London, U.K.

He is currently an Associate Professor with Chulalongkorn University, Bangkok, Thailand. He has authored or coauthored more than 100 technical papers in highly ranked journals and refereed conference proceedings. He has extensive experience in computational electromagnetics, notably in the area of finite-difference time-domain method for metamaterials. He also has experience in the ray tracing technique, the uniform theory of diffraction, and their applications in antenna engineering and radio propagation.

Dr. Zhao is a founding member of the Innovative Electromagnetic Academic of Thailand (iEMAT), and the Managing Editor for *Engineering Journal*. He was a regular reviewer for the IEEE TRANSACTIONS ON ANTENNAS AND PROPAGATION, IEEE ANTENNAS AND WIRELESS PROPAGATION LETTERS, IEEE MICROWAVE AND WIRELESS COMPONENTS LETTERS, *Progress in Electromagnetics Research*, and *Optics Express*.

Prayoot Akkaraekthalin (Member, IEEE) received the B.Eng. and M.Eng. degrees in electrical engineering from the King Mongkut's University of Technology North Bangkok (KMUTNB), Bangkok, Thailand, in 1986 and 1990, respectively, and the Ph.D. degree from the University of Delaware, Newark, DE, USA, in 1998.

From 1986 to 1988, he was a Research and Development Engineer with Microtek Company, Ltd., Bangkok, Thailand. In 1988, he joined the Department of Electrical Engineering at KMUTNB as an instructor and researcher. His current research interests include passive and active microwave circuits, telecommunications, and innovative sensor systems. He is the author and coauthor of more than 70 papers in international journals, more than 300 conference papers, and 6 books/book chapters.

Dr. Akkaraekthalin is a member of the IEEE, IEICE Japan, EEAAT and ECTI Thailand. He was the Chairman for the IEEE MTT/AP/ED Thailand Joint Chapter from 2007 and 2010. From 2011 to 2013, he was the Editor-in-Chief for the ECTI Transactions. From 2012 to 2013, he was the Vice-President of EEAAT association, Thailand, and, from 2012 to 2015, the Vice-President and the President of the ECTI Association, Thailand. He was the Leader of Senior Research Scholar Project of "Electromagnetic Applications for Sustainable Development of Thailand Industry" from 2014 to 2017 and "Innovative Sensor Technology using Electromagnetics for Thailand Development" from 2017 to 2020 granted by the Thailand Research Fund, Thailand.